(Revision 1: MS 7148)

REE redistributions during granite weathering: Implications for Ce anomaly as a proxy for paleoredox states

Koji Ichimura[1], Kenzo Sanematsu[2], Yoshiaki Kon[2], Tetsuichi Takagi[2] and Takashi Murakami[1,*]

[1]Department of Earth and Planetary Science, The University of Tokyo, 7-3-1 Hongo, Bunkyo-ku, Tokyo 113-0033, Japan

[2]Geological Survey of Japan, National Institute of Advanced Industrial Science and Technology, Central 7, 1-1-1 Higashi, Tsukuba, Ibaraki 305-8567, Japan

---

*Contact person: Takashi Murakami (murakami@eps.s.u-tokyo.ac.jp)

This is a preprint, the final version is subject to change, of the American Mineralogist (MSA)
Cite as Authors (Year) Title. American Mineralogist, in press.
DOI: https://doi.org/10.2138/am-2020-7148

19 **ABSTRACT**

20

21 Different response of Ce to redox state from those of the other light rare earth
22 elements (LREEs) can be used to understand paleoredox states. In order to establish the
23 possibility of using Ce anomaly as a proxy for paleo-environments, we examined the
24 mineralogical and chemical characteristics of bulk samples and REE-bearing minerals
25 of a modern weathering profile developed on granite, by X-ray fluorescence analysis,
26 laser-ablation inductively coupled plasma mass spectrometry, field emission electron
27 microprobe analysis, field emission scanning electron microscopy and X-ray
28 diffractometry. Bulk samples showed no significant Ce-anomalies except for the
29 topmost layer that had a positive Ce-anomaly reflecting significant loss of LREEs
30 except for Ce. Allanite-(Ce), primary REE-bearing mineral, contributed to ~100% of La,
31 Ce, Pr and Nd in the parent rock, and gradually decreased in amount toward the topmost
32 layer. Secondary cerianite-(Ce) ($Ce(IV)O_2$) was observed in the weathering profile,
33 especially at shallower depths. Secondary rhabdophane-(La), -(Ce), -(Nd) and -(Y) were
34 also observed in the weathering profile but in less amounts in the topmost layer. The
35 occurrences of rhabdophane-(La) and -(Nd) in contact with halloysite, secondary clay
36 mineral, suggest probable adsorption of REEs onto halloysite prior to their formation.

Similar formation mechanisms are likely for rhabdophane-(Ce) that commonly occurred in grain boundaries and was usually formed in contact with halloysite. Rhabdophane-(Y) occurred in association with fluorapatite. The ratios of La, Pr and Nd of rhabdophane-(La), -(Ce) and -(Nd) were similar to that of allanite-(Ce), suggesting that these LREEs are inherited from allanite-(Ce) and behave similarly before the formation of rhabdophane. Different negative Ce-anomaly values of rhabdophane (i.e., ~0.03–0.34 for rhabdophane-(La), -(Nd) and -(Y), and ~0.6 for rhabdophane-(Ce)) can result from a difference in intensity of the formation of cerianite-(Ce) prior to the precipitation of rhabdophane. We have classified LREE redistributions in both secondary minerals and bulk weathered samples during oxic weathering and suggested that Ce anomaly can provide useful information on anoxic weathering and thus atmospheric oxygen evolution in the Precambrian if Ce anomalies of both bulk samples and secondary REE-bearing minerals are determined.

Keywords: REE, weathering, Ce anomaly, paleoredox and phosphate

This is a preprint, the final version is subject to change, of the American Mineralogist (MSA)
Cite as Authors (Year) Title. American Mineralogist, in press.
DOI: https://doi.org/10.2138/am-2020-7148

54 **INTRODUCTION**

55

56 Because weathering is mineral-water-atmosphere interaction, geological records of
57 paleoweathering provide useful information on paleo-environments, especially
58 atmospheric oxygen and carbon dioxide concentrations (Holland et al. 1984; Rye and
59 Holland 1998; and references therein). Chemical analyses of rare earth elements (REEs)
60 have been applied to paleosols, ancient weathering soils, to understand
61 paleo-environments (e.g., Wiggering and Beukes 1990; Macfarlane et al. 1994; Pan and
62 Stauffer 2000; Panahi et al. 2000; Murakami et al. 2001; Yang et al. 2002; Yang and
63 Holland 2003; Utsunomiya et al. 2003; Ichimura and Murakami 2009), using Ce
64 anomaly ($Ce/Ce^* = Ce_N/(La_N \times Pr_N)^{1/2}$ where $Ce \equiv Ce_N$ and $Ce^* \equiv (La_N \times Pr_N)^{1/2}$, and
65 REE_N is the REE concentration normalized by CI chondrite (McDonough and Sun
66 1995)). Earlier studies (Sawka et al. 1986; Banfield and Eggleton 1989; Braun et al.
67 1990; Braun et al. 1993; Cotten et al. 1995) have reported that Ce fractionation occurs
68 in modern, oxic weathering as follows: cerianite-(Ce) ($Ce(IV)O_2$) is formed through
69 Ce(III) oxidation and subsequently rhabdophane with negative Ce-anomalies is formed,
70 utilizing dissolved P and REEs from primary minerals such as apatite and allanite. Such
71 Ce fractionation has been considered to result from a difference in mobility between

Ce(IV) and other trivalent LREE including Ce(III) and to be evidence of the presence of a significant amount of atmospheric oxygen. Then the absence or presence of Ce anomaly has been applied to paleosols to determine whether the paleosols were formed under oxic or anoxic conditions (e.g., Wiggering and Beukes 1990; Macfarlane et al. 1994).

On the other hand, the above Ce fractionation processes under oxic conditions may be further complicated by i) Ce(III) oxidation by oxyhydroxide-assisted scavenging (e.g., Janots et al. 2015) and by microbial mediation (Moffett 1990; 1994), ii) suppression of Ce(III) oxidation by organic complexation (e.g., Davranche et al. 2004; 2005; Yu et al. 2018) and iii) enhancement of rhabdophane formation by biological processes (e.g., Taunton et al. 2000). Furthermore, mere absence or presence of Ce anomaly may not simply determine paleoredox conditions during weathering because of various formations of Ce anomalies shown by more recent studies: (1) erosion of the upper layer of a paleosol could result in the absence of Ce anomaly even if a Ce anomaly could have been present in the upper layer that disappeared (Pan and Stauffer 2000); (2) a Ce anomaly could be obscured on a meter scale even if Ce could have been separated from the other LREEs on a mm to cm scale (Lottermoser 1990); (3) a Ce anomaly could not be necessarily related to the oxidation state of Ce if the

transportation of the other LREEs than Ce from the upper layer could have changed the Ce anomaly sign from zero to negative in the deeper layer (e.g., Takahashi et al. 2000; Janots et al. 2015); (4) the abundance ratios of LREEs could not change significantly if primary REE-bearing minerals could have not been dissolved significantly (Takahashi et al. 2000; Sanematsu et al. 2015); (5) later metasomatism and/or metamorphism could alter the chemical compositions of some minerals, including that of rhabdophane, having formed at the time of weathering (e.g., Fedo et al. 1997; Ichimura and Murakami 2009); and (6) rhabdophane with the absence of Ce anomaly could form under oxic conditions (Nagy et al. 2002; Berger et al. 2014; Liu et al. 2016). These limitations make it difficult to interpret Ce anomalies of Precambrian paleosols especially because REE concentrations have been mostly measured for bulk samples but not for REE-bearing minerals (e.g., Ichimura and Murakami 2009).

Despite the above limitations in the application of Ce anomaly to the determination of redox states of paleo-environments, the present study has been undertaken to clarify how REEs are redistributed in bulk samples and secondary REE-bearing minerals depending on either oxic or anoxic conditions, which is useful to understand atmospheric oxygen evolution in the Precambrian. To reach these goals we have examined mineralogical and chemical aspects of a modern weathering profile and

primary and secondary REE-bearing minerals.

SAMPLES AND METHODS

Samples

A weathering profile of granite located in Inada, Ibaraki, central Japan (36˚22'N 140˚11'E) was studied. The radiogenic age of the Inada granite is 60−65 Ma (Arakawa and Takahashi 1988 and references therein). The granite is coarse-grained, and composed of quartz, plagioclase, orthoclase and biotite as major minerals, and allanite, zircon, apatite and ilmenite as accessory minerals (Arakawa and Takahashi 1988). The samples for the present study were exposed on the steep edge of a small table land; six weathered samples (YMK1, at a depth of 5.0 m from the surface of the table land; YMK2, 10.4 m; YMK3, 19.2 m; YMK4, 25.0 m; YMK5, 29.0 m; and YMK6, 31.0 m), and one fresh granite sample (YMK7) were collected. The location of the samples in the profile is given in Fig. 1. The subsurface soils were mixed with plant roots and therefore not sampled.

Analytical methods

Whole-rock chemical compositions of the bulk samples were determined by X-ray fluorescence analysis (XRF, PANalytical, Axious) and laser-ablation inductively coupled plasma mass spectrometry (LA-ICP-MS, Cyber Laser Inc., IFRIT and Agilent Technologies, Agilent 7500cx). The major and clay mineral species were identified by X-ray diffractometry (XRD, Rigaku, RINT 2100 and PANalytical, X'Pert Pro MPD). The chemical compositions of individual minerals were determined by field emission electron microprobe analysis (EMPA, JEOL, JXA-8530F). The species, occurrences, textures and morphologies of minerals on a μm scale were examined by field emission scanning electron microscopy (SEM, Hitachi, S4500) equipped with an energy dispersive X-ray spectrometer (EDS, Kevex system) and an electron backscatter diffraction analyzer (EBSD, ThermoNoran, Phase ID system). Modal compositions of the bulk samples were determined using SEM and XRD.

X-ray fluorescence analysis. For whole-rock chemical analyses, bulk samples >~200 g were dried at room temperature and the amount was reduced by the coning and quartering method (McNaught and Wilkinson 1997). Note that sample YMK7 (fresh granite) was crushed by an Fe-Mn alloy jaw crusher prior to the amount reduction. Each sample of 40 g was pulverized by a vibration mill (TI-100, CMT) with an alumina container and rod for 3 min. Each powder sample was heated at 1000 °C for 2 h to

144 measure loss on ignition (LOI). A glass bead sample for XRF measurement was
145 prepared by mixing 0.5 g of each powder sample with 5.0 g of di-lithium tetraborate
146 ($Li_2B_4O_7$, Spectromelt A10) flux. This mixture was heated to 1150 ˚C for 8 min in a
147 95% Pt-5% Au crucible of 30 mm of inner diameter, using an automatic high frequency
148 bead sampler (TK-4100, Tokyo-Kagaku Co., Ltd.). Major element compositions of the
149 bulk samples were determined by XRF. The operating voltage and current of the Rh
150 X-ray tube were 50 kV and 50 mA, respectively. Analytical error was estimated by
151 counting the statistical error of each element. Calibration lines of the major elements
152 were established using the Geological Survey of Japan (GSJ) geochemical reference
153 samples of igneous rock series (Imai et al. 1995, 1999; Terashima et al. 1998).
154 **Laser-ablation inductively coupled plasma mass spectrometry**. The XRF
155 glass-bead samples were used to measure the trace element compositions by
156 LA-ICP-MS (Kon et al. 2011). The carrier-gas flow rate and ion-lens setting of ICP-MS
157 were adjusted carefully to maximize the S/N ratio of La and to minimize the oxide
158 production rate ($^{232}Th^{16}O/^{232}Th$). The laser system was operated with a 780 nm light
159 source, a ~20 μm diameter pit size, 100 $\mu J/cm^2$ pulse energy, a 1000 Hz pulse repetition
160 rate and 90 sec ablation. In order to minimize elemental fractionation during ablation
161 and to ablate the glass-bead samples effectively, the ablation spot was moved at 500

μm/sec throughout the analysis. For all elements analyzed, Si-normalized signal intensities were calibrated using three GSJ reference materials (JB-3, JG-3 and JR-3; Imai et al. 1995, 1999). The uncertainties were <~10% for each element. The chemical compositions of the major and trace elements of the bulk samples are listed in Table 1.

X-ray diffractometry. The bulk samples were powdered by milling with tungsten carbide and the constituent minerals were identified by XRD. The modal compositions of the major minerals in the weathering profile were determined by XRD based on the modal compositions of respective minerals in the parent rock (see the section of scanning electron microscopy). We made another set of powder samples for the modal composition determination because biotite is much less resistant to mechanical milling than quartz, which can affect the XRD intensities. Quantitative modal compositions were determined by the following procedures (cf., Nelson and Cochrane 1970): 2 g of each sample was powdered by milling with tungsten carbide for 30 sec, mixed with 20 wt% of α-Al_2O_3 particles of 1 μm in diameter as a quantitative standard, and subjected to XRD. The modal compositions of quartz, plagioclase, orthoclase and biotite in the weathered samples (samples YMK1−6) were determined according to the ratios of the intensities at 100, $20\bar{1}$, $20\bar{1}$ and 001 reflections, respectively, to those of the parent rock (sample YMK7). The residue was assumed to be ascribed to the fraction of clays

for each weathered sample while the clay (including amorphous phase) content of the parent rock was assumed to be zero.

The bulk samples were gently crushed by hand in water (for samples YMK1−4) or by mechanical milling (for samples YMK5−7) for identification of clay minerals. A < 2 μm fraction was separated from each powder sample by elutriation, and then, its oriented specimen was subjected to XRD. Halloysite was distinguished from kaolinite by treating the < 2 μm fraction with hydrazine, water and glycerol (e.g., Range et al. 1969). Chlorite, smectite and vermiculite (peaks at around 1.4 nm) were distinguished from one another by the treatment of the < 2 μm fraction with ethylene glycol and heating (500 ˚C). The qualitative amounts of clay minerals were obtained from their peak intensities.

Electron microprobe analysis. Polished thin sections of the bulk samples were made for chemical analyses by EMPA; the operating voltage was 25 kV and the beam current 50 nA, which resulted in ~3 μm in size for the analyzed area of a specimen. The standards used were: LaB_6 for B; CaF_2, F; albite, Na; MgO, Mg; Al_2O_3, Al; $CaSiO_3$, Si and Ca; sodalite, Cl; adularia, K; TiO_2, Ti; VO_2, V; chromite, Cr; Mn_2SiO_4, Mn; hematite, Fe; NiO, Ni; $SrSO_4$, S and Sr; $Y_3Al_5O_{12}$, Y; ZrO_2, Zr; REE phosphate (Cherniak et al. 2004), P and lanthanides (La−Lu); HfO_2, Hf; and (Pb, V, Ge) oxide, Pb.

198 The standards indicated by chemical formulas are those synthesized. Thorianite and
199 uraninite whose compositions were measured by SEM-EDS (JEOL, JSM-5310 for SEM
200 and Oxford, Link ISIS for EDS) prior to the EMPA measurements were used for the
201 standards for Th and U, respectively. The backgrounds were corrected according to
202 Williams (1996) for Cr, Mn, Fe, Ni, Pr, Sm, Eu, Gd, Tb, Dy, Ho, Er, Tm, Yb and Lu,
203 and for the other elements, corrected using the backgrounds near the corresponding
204 peaks. We also corrected for peak overlaps (e.g., at Eu(Lα)-La($L\gamma_1$), Pr($L\beta_2$), Nd($L\beta_2$)).
205 After the corrections, the peak intensities were corrected for ZAF. Note that secondary
206 REE-bearing minerals were fine (see below), and therefore, their aggregates of >~5 μm
207 in size were analyzed by EMPA. The concentrations of individual REEs contained in
208 the standard REE phosphate were 0.1−1wt% as REE_2O_3 and the relative measurement
209 uncertainties and detection limits were 0.01−0.05wt% and 0.05−0.15wt% as REE_2O_3,
210 respectively. The REE-bearing minerals contained in the samples are listed in Table 2
211 with their ideal formulas, and their chemical compositions are summarized in Tables 3
212 and 4 for the parent and weathered rocks, respectively.

213 **Scanning electron microscopy**. SEM, including secondary and backscattered
214 electron imaging, of < 2 μm fractions, polished thin sections and fracture surfaces of the
215 samples was used to examine the occurrences, textures and morphologies of minerals.

SEM-EBSD was used for mineral identification with software developed by Kogure (2003).

Backscattered electron micrographs of five polished thin sections with an area of ~30 cm^2 in total were used to measure the areas (in pixels) of the major minerals (i.e., quartz, plagioclase, orthoclase and biotite) in the parent rock (sample YMK7) and to determine their modal compositions. The areas of REE-bearing mineral particles were measured in the same way as above for the modal compositions of primary REE-bearing minerals except for zircon and fluorapatite in the parent rock, and for the average chemical compositions of both primary and secondary REE-bearing minerals (see below). The modal compositions of zircon and fluorapatite were calculated from the whole-rock concentrations of Zr and P, respectively, in the parent rock (Table1) because we could reasonably assume that all Zr and P were only contained in zircon and fluorapatite, respectively.

RESULTS

Weathering and mineralogy in the profile

Changes in LOI and chemical index of alteration (CIA ≡ {Al_2O_3/(Al_2O_3 + CaO +

234 $Na_2O + K_2O)\}x100$ (in moles); Nesbitt and Young 1982) indicated that weathering was
235 generally stronger at shallower depths toward the top of the profile, which was
236 confirmed by decreases in Na and Ca with depth (Fig. 2). In contrast, large changes
237 were not found in the compositions of major elements except for Na and Ca or trace
238 elements through the weathering profile (Table 1).

239 The modal composition of major minerals in the parent rock was: 32.3(±1.8)wt%
240 quartz, 39.7(±1.5)wt% plagioclase, 22.7(±1.0)wt% orthoclase and 5.1(±0.4)wt% biotite.
241 Quartz and orthoclase persisted without a decrease in content even at the top of the
242 profile while plagioclase decreased its content with depth and biotite almost disappeared
243 at depths of < 20 m (Fig. 1). The decrease in plagioclase with depth is consistent with
244 similar decreases in Na_2O and CaO (Figs. 1 and 2). Clay minerals observed in the
245 weathering profile were halloysite, kaolinite, smectite and vermiculite. Halloysite and
246 kaolinite were observed at depths of < 25 m and smectite/vermiculite at depths of < 29
247 m (Fig. 1). Figure 3 demonstrates the presence of halloysite and that of kaolinite, though
248 less in amount, in sample YMK2; the 1.03 and 0.72 nm peaks (Fig. 3a) converged to a
249 1.04 nm peak (with a faint peak at 0.72 nm) after hydrazine treatment (Fig. 3b), the 1.04
250 nm peak showed higher intensity after the hydrazine-treated specimen was washed by
251 water (Fig. 3c), a 1.11 nm peak, indicating the presence of halloysite, appeared by

glycerol treatment of the hydrazine/water-treated specimen (Fig. 3d), and finally a 1.00 nm peak (biotite) remained after heat treatment (Fig. 3e). Tubular morphology, characteristic of halloysite, was observed by SEM. The clay fraction increased with depth (Fig. 1).

REEs in the bulk samples

The concentrations of total REEs and LREEs (ΣREE and ΣLREE, respectively) were similar throughout the weathering profile or faintly increased with depth except for those in the uppermost sample (YMK1) where they were slightly lower than and similar to, respectively, those in the parent rock (Fig. 2). Ce anomalies were almost absent at depths of >10 m while sample YMK1 at a depth of 5.0 m showed a positive Ce-anomaly (Fig. 2). The concentration of total HREEs (ΣHREE) was generally smaller in the weathered samples than that in the parent rock (Fig. 2), which is usually observed for granite weathering (e.g., Nesbitt 1979).

The REE patterns of the weathered samples except for sample YMK1 were characterized by slightly higher LREE and lower HREE concentrations than those of the parent rock (Fig. 4a), which is commonly observed for weathering of granite (e.g., Nesbitt 1979; Braun et al. 1990; Aubert et al. 2001). The REE pattern of sample YMK1

showed lower REE concentrations than those in the parent rock except for Ce with a positive anomaly (Fig. 4a). This trend is emphasized when the REE concentrations are normalized by those of the parent rock (Fig. 4b). All REE patterns were accompanied by negative Eu-anomalies (Fig. 4a). The Ce anomaly was significant only in sample YMK1 but not for the other samples (Figs. 2 and 4a). The characteristics shown in the REE patterns generally coincide with the depth variations shown in Fig. 2 (e.g., the depth variation of ΣREE).

Occurrences of REE-bearing minerals

Allanite-(Ce) was apparently major and other LREE-bearing minerals such as xenotime-(Y) and fluorapatite were minor for contributions to LREEs of the parent rock (Table 3). The qualitative abundances of primary REE-bearing minerals in the weathering profile are given in Table 5. Allanite-(Ce) started to be dissolved at a depth of 25.0 m and was low in amount at depths of 10.4 m and shallower. The qualitative depth-profile of the allanite-(Ce) abundance in Table 5 is apparently a mirror image of those of LOI and CIA in Fig. 2, suggesting that allanite-(Ce) was weathered in a similar trend to that of the whole weathering profile. Fluorapatite, a source of phosphorous for secondary REE phosphates, was a common REE-bearing mineral in the parent rock and

288 also present in the weathering profile but just as trace abundance at depths of <25 m.
289 Xenotime-(Y) was occasionally observed.

290 The qualitative abundances of secondary REE-bearing minerals in the weathering
291 profile are given in Table 5. Cerianite-(Ce) was observed throughout the whole
292 weathering profile, even at depths of 31 and 29 m, and most abundant at a depth of 5.0
293 m (sample YMK1). The cerianite-(Ce) abundance at 5.0 m is reflected in the REE
294 pattern where only Ce is apparently enriched compared to the other LREEs (Fig. 4b).
295 Cerianite-(Ce) occurred in small veins or grain boundaries usually with Mn
296 (oxyhydr)oxide (Figs. 5a and 5b). Rhabdophane was similarly observed at depths of
297 25−10 m but of trace at a depth of 5.0 m (Table 5). Rhabdophane occurred as aggregates
298 of fine crystals with widths of several tens to several hundreds of nm and lengths of
299 several tens of nm to 5 μm (Fig. 5c). Rhabdophane was classified into
300 rhabdophane-(La), rhabdophane-(Ce), rhabdophane-(Nd) and rhabdophane-(Y).
301 Rhabdophane-(La) mainly occurred in veins in weathered plagioclase, in contact with
302 halloysite (Fig. 5d; “Kl” is probably halloysite). Rhabdophane-(Ce) mainly occurred in
303 grain boundaries, usually associated with halloysite (Fig. 5e; “Kl” is probably
304 halloysite). Rhabdophane-(Nd) was observed in veins in weathered plagioclase,
305 associated with halloysite (Fig. 5f), and also observed occasionally accompanied by

306 smectite and associated with fluorapatite (Fig. 5g). Rhabdophane-(Y) was found only in
307 sample YMK6, occurring similarly to the latter type of the occurrence of
308 rhabdophane-(Nd) (Fig. 5h). Rhabdophane commonly had elongated shapes, identified
309 by comparing the EBSD patterns (e.g., Fig. 5i) to the calculated ones (e.g., Fig. 5j). The
310 kaolin minerals shown in Fig. 5 were probably halloysite since there were relatively
311 larger amounts of halloysite than kaolinite in samples YMK2 and YMK4 (at depths of
312 10.4 and 25.0 m, respectively; Fig. 1) and they appeared rod shaped under SEM (data
313 not shown). Halloysite domains isolated from rhabdophane ones were analyzed by
314 EMPA to measure REE concentrations adsorbed onto halloysite, but the concentrations
315 of individual REEs on halloysite were under the detection limits (i.e., <0.05–0.15wt%).
316

317 **Chemical compositions of REE-bearing minerals**

318 We could not give a complete set of quantitative REE compositions of either
319 primary or secondary REE-bearing minerals because the concentrations of some REEs
320 were low and sometimes below detection limits (Tables 3 and 4). Despite incomplete
321 chemical information, the REE compositions of both primary and secondary
322 REE-bearing minerals provide important information on the REE transport as discussed
323 below. The average compositions shown in Tables 3 and 4 were calculated by the

equation below:

$$C_{n,Z} = \sum_{ni}\left(A_{ni}C_{ni,Z}\right)/\sum_{ni} A_{ni} \quad (1)$$

where $C_{n,Z}$ is the average concentration of element Z in mineral species n (wt%), A_{ni} the area of an individual particle ni of mineral species n (pixel number, dimensionless), and $C_{ni,Z}$ the concentration of element Z in an individual particle ni of mineral species n (wt%). See Section "Analytical methods" for the measurements of A_{ni}.

The chemical compositions of REE-bearing minerals in the parent rock show how REEs were individually distributed in the minerals (Fig. 6a). Being apparently the major LREE-bearing mineral, LREEs were mostly contained in allanite-(Ce) which, however, did not have significant amounts of HREEs (compare the REE pattern of allanite-(Ce) to that of the bulk parent rock in Fig. 6a). HREEs were instead contained in allanite-(Y), fluorapatite, zircon, xenotime-(Y), Ca- and Y-rich unidentified phase, titanite and epidote (Fig. 6a). All primary REE-bearing minerals had large negative Eu-anomalies (Table 3 and Fig. 6a).

The chemical compositions of the secondary REE-bearing minerals are given in Table 4, and the REE patterns of rhabdophane are shown in Fig. 6b compared to those of allanite-(Ce) of the parent rock and bulk sample YMK2. The REE pattern of only sample YMK2 is given as an example of those of the weathered samples except for

342 sample YMK1. Figure 6b shows that the slopes of the LREE patterns of
343 rhabdophane-(La), -(Ce) and -(Nd) were similar to that of allanite-(Ce) if we exclude
344 the Ce anomalies from the slopes. Rhabdophane-(Y) had a different slope from those of
345 rhabdophane-(La), -(Ce) and -(Nd). Rhabdophane-(La), -(Ce) and -(Nd) shared similar
346 slopes of HREE patterns. The rhabdophanes had different values of Ce anomaly from
347 one another despite the absence of Ce anomaly in allanite-(Ce) (Fig. 6b).
348 The slopes of LREE patterns (LREEs except for Ce) of rhabdophane-(La), -(Ce)
349 and -(Nd) were similar to that of bulk weathered sample YMK2 (Fig. 6b), which
350 suggests a significant contribution of rhabdophane to the LREE redistribution during
351 weathering. The values of Ce anomaly of rhabdophane were less than one (Table 4)
352 although those of the bulk samples were nearly one or more (Table 1), suggesting
353 significant fractionation of Ce between cerianite-(Ce) and rhabdophane. The values of
354 Eu anomaly of rhabdophane were much smaller than those of the bulk samples (Tables
355 1 and 4).
356
357 **DISCUSSION**
358
359 Before we discuss the role of rhabdophane in REE redistribution, we briefly

summarize our results of the mineralogy and chemistry of the weathering profile of the Inada granite. The intensity of weathering is slightly greater at shallower depths as indicated by the parameters such as the abundances of plagioclase and biotite, the values of CIA and the concentrations of Na_2O and CaO (Figs. 1 and 2). The concentrations of ΣREE and ΣLREE are similar throughout the weathering profile or faintly increase toward the top of the profile but decrease at the uppermost layer, sample YMK1; Ce anomalies are absent throughout the profile except for the uppermost layer (Fig. 2). The characteristics of the uppermost layer are distinct from those of samples YMK2 to YMK6 as shown in Fig. 4b by the similar abundances of Ce and the lower abundances of the other LREEs, suggesting vertical transport of LREEs except for Ce.

The high abundances of rhabdophane at depths of 10.4 and 25.0 m are in accordance with those of halloysite at the same depths (Fig. 1 and Table 5). Indeed, rhabdophane-(La), -(Ce) and -(Nd) usually occur in association with halloysite (Figs. 5d, 5e and 5f). Among the rhabdophanes, rhabdophane-(Y) is found only in smectite of sample YMK6, usually accompanied by fluorapatite (Fig. 5h). The primary LREE-bearing mineral, allanite-(Ce), shows no Ce-anomaly (Table 3) while secondary rhabdophane-(La) and -(Nd) have large negative Ce-anomalies (~0.20 and 0.06, respectively, Table 4) and rhabdophane-(Ce) has small negative Ce-anomalies (~0.62,

Table 4). Although we failed to obtain evidence of LREE adsorption on halloysite, LREE adsorption on kaolin minerals and association of rhabdophane with kaolin minerals have been reported (e.g., Seredin and Dai 2012). It is likely that LREE adsorption on halloysite and subsequent rhabdophane formation occur in the weathering profile. Cerianite-(Ce) is precipitated with little relation to the halloysite occurrences (Figs. 5a and 5b). Therefore, LREEs in solution are fractionated after cerianite-(Ce) is formed, and LREEs adsorbed on halloysite are probably deficient in Ce compared to other LREEs especially La and Nd.

We here consider the transport pathways of REEs from the primary REE-bearing minerals to the secondary REE-bearing minerals. Firstly, we examine REE fractional contributions of the primary REE-bearing minerals to respective REE concentrations in the parent rock. The fractional contribution of element Z in mineral species n to element Z in the whole parent rock, $f_{n,Z}$ (%), can be calculated by the following equation:

$$f_{n,Z} = C_{n,Z}\delta_n / C_{rock,Z} \quad (2)$$

where $C_{rock,Z}$ is the concentration of element Z in the parent rock (wt%), and δ_n the modal composition of mineral species n (wt%). δ_n is obtained from

$$\delta_n = 100\,\rho_n V_n / \sum_n(\rho_n V_n) \cong 100\rho_n A_n / \sum_n(\rho_n A_n) \quad (3)$$

where ρ_n is the density of mineral species n (g·m^{-3}), V_n the volume (m^3) of mineral

396 species *n* and A_n the total area of mineral species *n* (pixel number, dimensionless;
397 $A_n = \sum_{ni} A_{ni}$). The δ_n values or modal compositions of the primary REE-bearing
398 minerals are given in Table 3.

399 Figure 7 shows the REE fractional contributions of the primary REE-bearing
400 minerals to their respective REE concentrations in the parent rock. Allanite-(Ce)
401 contributes to ~100% of La, Ce, Pr and Nd, ~90% of Sm and ~40% of Gd in the parent
402 rock, which should be compared to, for instance, ~50% ΣLREE contribution of allanite
403 to the ΣLREE concentration of the whole-rock of parent gneiss (Braun et al. 2018). The
404 domination of allanite-(Ce) for La, Ce, Pr, Nd and Sm is, therefore, of advantage to
405 estimate their fates in the weathering profile. We can reasonably assume that almost all
406 La, Ce, Pr and Nd and most of Sm in the secondary REE-bearing minerals and in the
407 weathering profile originate from allanite-(Ce). Allanite-(Y) contributes to ~20–50% of
408 Y and HREEs, and fluorapatite ~30–40% of Y and HREEs at maximum. Some of the
409 remaining HREEs and/or Y are ascribed to zircon, titanite and Ca- and Y-rich
410 unidentified phase. Although we successfully attributed ~100% of La, Ce, Pr and Nd
411 and ~90% of Sm to allanite-(Ce), we attributed nearly less than 50% for most of the rest
412 of REEs to individual, primary REE-bearing minerals (Fig. 7).

413 We next examine the ratios of individual REEs of rhabdophane to respective ones

414 of allanite-(Ce). Because rhabdophane is a phosphate and allanite is a silicate, we
415 compare their REE concentration ratios by normalizing the REE concentration ratios by
416 the ΣREE ratio of the two minerals (see the caption of Fig. 8 for the detail of the
417 calculation). Figure 8a shows that the proportions of La, Pr and Nd of rhabdophane are
418 similar to that of allanite-(Ce) but Ce is deficient in rhabdophane compared to
419 allanite-(Ce) (also see Tables 3 and 4). Because La, Ce, Pr and Nd of the parent rock,
420 sample YMK7, are almost all ascribed to allanite-(Ce), the similar proportions of La, Pr
421 and Nd strongly suggest that La, Pr and Nd are transported and precipitated by similar
422 mechanisms during weathering. The deficiency of Ce in rhabdophane is caused by Ce
423 fractionation through Ce(IV) precipitation as cerianite-(Ce) in other areas of the same
424 layer because no Ce-anomaly is observed in the bulk samples except for sample YMK1
425 which shows an apparent Ce enrichment resulting from the leaching of the other LREEs
426 (Fig. 4b). The four rhabdophanes have different values of Ce anomaly (Table 4). Further,
427 rhabdophane particles have a variety of Ce-anomaly values (Fig. 8b). The variety of
428 Ce-anomaly values in rhabdophane particles in the same layer can be possibly caused
429 by different amounts of dissolved Ce among localities due to different amounts of
430 cerianite-(Ce) precipitates, which is consistent with similar Nd/La concentration ratios
431 in the rhabdophane particles (Fig. 8c). Thus, even if there is no Ce-anomaly in bulk

samples, rhabdophane particles can have a variety of Ce anomalies under oxic weathering by Ce fractionation. The formation mechanisms of rhabdophane-(Y) are probably different from those of the other types of rhabdophane, suggested by the differences in occurrence (found only in sample YMK6, Table 5) and in REE pattern (Fig. 6b).

IMPLICATIONS

Previous studies have reported that negative Ce-anomaly of a weathering profile does not necessarily reflect oxic weathering (e.g., Takahashi et al. 2000), the absence of Ce anomaly in secondary REE-bearing minerals such as rhabdophane does not necessarily reflect anoxic weathering (e.g., Janots et al. 2015), and Ce(III) oxidation can be suppressed under oxic conditions in organic-rich environments (e.g., Yu et al. 2018). However, the present study has revealed that we can observe records of oxidations in secondary REE-bearing minerals with Ce fractionation if we examine both primary/secondary REE-bearing minerals and bulk rocks. We show below whether a certain weathering profile has occurred under oxic or anoxic conditions using Ce anomaly.

Nearly 100% of La, Ce, Pr and Nd in the parent rock are contained in allanite-(Ce) (Fig. 7), and therefore, the release rates of these four elements to solution should be almost the same. Accordingly, we only need to consider differences in reaction pathways between these elements prior to the precipitation of rhabdophane to explain the behaviors of these elements during oxic weathering. The reaction pathways among La, Pr and Nd are probably similar (Fig. 8c) while Ce behaviors prior to the precipitation of rhabdophane are different as indicated by the variable negative Ce-anomalies in rhabdophane (Fig. 8b). Sample YMK1, the topmost layer, has a positive Ce-anomaly but the other bulk samples have no Ce-anomaly (Fig. 4a). This Ce fractionation occurs by the preferential removal of trivalent LREEs compared to Ce(IV), which is consistent with the fact that the abundance of cerianite-(Ce) is common but those of rhabdophane-(La), -(Ce) and -(Nd) are at trace levels in the topmost layer (Table 5).

Our discussion and previous studies (given below) indicate that we can classify the LREE redistributions between minerals during oxic weathering as follows (Fig. 9): i) presence of rhabdophane with a negative Ce-anomaly and the presence of cerianite-(Ce) in the same bulk layer that has no Ce-anomaly (e.g., Lottermoser et al. 1990), ii) presence of rhabdophane with a negative Ce-anomaly in one layer and the presence of

468 cerianite-(Ce) in another layer that has a positive Ce-anomaly (e.g., Braun et al. 1998),
469 and iii) presence of rhabdophane with almost no Ce-anomaly in one layer and the
470 presence of cerianite-(Ce) in another layer that has a positive or negative Ce-anomaly
471 (e.g., Janots et al. 2015). In cases ii and iii, rhabdophane and cerianite-(Ce) can coexist
472 in one layer where their relative abundances vary significantly (Fig. 9). In any cases,
473 cerianite-(Ce) must form during oxic weathering. Then, the above LREE redistributions
474 during oxic weathering can imply redistributions of LREEs, especially Ce behavior,
475 during anoxic weathering in the Precambrian as follows: cerianite-(Ce) is not formed
476 because its formation must be accompanied by oxidation of Ce(III) through atmospheric
477 oxygen when the effects of biota on weathering are insignificant (Berner 1992; Algeo
478 and Scheckler 1998). Because Mn-oxide formation itself is evidence of oxic weathering
479 (e.g., Hem 1963; Yang and Holland 2003; Murakami et al. 2011), Ce(III) oxidation and
480 cerianite-(Ce) formation on the surface of Mn oxides (e.g., Taylor and McLennan 1988;
481 Takahashi et al. 2007; Nakada et al. 2013) also occur under oxic conditions. Because Ce
482 is transported as Ce(III) in solution in a similar pathway to that of the other LREEs
483 without oxidation, either rhabdophane or bulk layers have no Ce-anomaly in any
484 horizons of a weathering profile.

485 Nonetheless, the above criteria of LREE redistribution in anoxic weathering have

rarely been applied to paleosols for the examination of paleoredox conditions (Murakami et al. 2001; Ichimura and Murakami 2009), mainly because paleosols have been subjected to later metasomatism and/or metamorphism which have altered some minerals probably including rhabdophane. Rhabdophane is easily altered to monazite even under low-temperature metasomatism or metamorphism (e.g., Jonasson and Vance 1986), and therefore, rhabdophane formed in Precambrian weathering has been altered and exists as monazite in paleosols as suggested by Ichimura and Murakami (2009). If original rhabdophane with no Ce-anomaly is formed under anoxic conditions, the secondary monazite is expected to inherit the absence of Ce anomaly. Not only monazite but also bulk layers have no Ce-anomaly if weathering occurred under anoxic conditions. We suggest that such examination can shed light on atmospheric oxygen evolution in the Precambrian.

ACKNOWLEDGMENTS

We are grateful to K. Putirka, Editor, J.-J. Braun and one anonymous reviewer for the earlier version and A. Fernandez-Martinez, Editor, and three anonymous reviewers for the present version. Their useful comments have greatly improved the quality of the

manuscript. This work was partly supported by Grant-in-Aids of the Ministry of Education, Culture, Sports, Science and Technology – Japan to TM (#24340132 and #15K05338).

REFERENCES CITED

Algeo, T. and Scheckler, S. (1998) Terrestrial-marine teleconnections in the Devonian: Links between the evolution of land plants, weathering processes, and marine anoxic events. Philosophical Transactions of the Royal Society B-Biological Sciences, 353, 113-128.

Arakawa, Y. and Takahashi, Y. (1988) Rb-Sr ages of granitic rocks from the Tsukuba district, Japan. Journal of Mineralogy, Petrology and Economic Geology, 83, 232-240.

Aubert, D., Stille, P. and Probst, A. (2001) REE fractionation during granite weathering and removal by waters and suspended loads: Sr and Nd isotopic evidence. Geochimica et Cosmochimica Acta, 65, 387-406.

Banfield, J.F. and Eggleton, R.A. (1989) Apatite replacement and rare-earth mobilization, fractionation, and fixation during weathering. Clays and Clay Minerals, 37, 113-127.

Berger, A., Janots, E., Gnos, E., Frei, R. and Bernier, F. (2014) Rare earth element mineralogy and geochemistry in a laterite profile from Madagascar. Applied Geochemistry, 41, 218-228.

Berner, R. (1992) Weathering, plants, and the long-term carbon-cycle. Geochimica et Cosmochimica Acta, 56, 3225-3231.

Braun, J.-J., Pagel, M., Muller, J.P., Bilong, P., Michard, A. and Guillet, B. (1990) Cerium anomalies in lateritic profiles. Geochimica et Cosmochimica Acta, 54, 781-795.

Braun, J.-J., Pagel, M., Herbillon, A. and Rosin, C. (1993) Mobilization and redistribution of REEs and thorium in a syenitic lateritic profile - a mass-balance study. Geochimica et Cosmochimica Acta, 57, 4419-4434.

Braun, J.-J., Viers, J., Dupré, B., Polve, M., Ndam, J. and Muller, J.P. (1998) Solid/liquid REE fractionation in the lateritic system of Goyoum, east Cameroon: The implication for the present dynamics of the soil covers of the humid tropical regions. Geochimica et Cosmochimica Acta, 62, 273-299.

Braun, J.-J., Riotte, J., Battacharya, S., Violette, A., Oliva, P., Prunier, J., Marechal, J., Ruiz, L., Audry, S. and Subramanian, S. (2018) REY-Th-U dynamics in the Critical Zone: Combined

535 influence of reactive bedrock accessory minerals, authigenic phases, and hydrological sorting
536 (Mule Hole Watershed, South India). Geochemistry Geophysics Geosystems, 19, 1611-1635.

537 Cherniak, D.J., Pyle, J. and Rakovan, J. (2004) Synthesis of REE and Y phosphates by Pb-free
538 flux methods and their utilization as standards for electron microprobe analysis and in design of
539 monazite chemical U-Th-Pb dating protocol. American Mineralogist, 89, 1533-1539.

540 Cotten, J., Ledez, A., Bau, M., Caroff, M., Maury, R.C., Dulski, P., Fourcade, S., Bohn, M. and
541 Brousse, R. (1995) Origin of anomalous rare-earth element and yttrium enrichments in
542 subaerially exposed basalts: Evidence from French-Polynesia. Chemical Geology, 119,
543 115-138.

544 Davranche, M., Pourret, O., Gruau, G. and Dia, A. (2004) Impact of humate complexation on
545 the adsorption of REE onto Fe oxyhydroxide. Journal of Colloid and Interface Science, 277,
546 271-279.

547 Davranche, M., Pourret, O., Gruau, G., Dia, A. and Le Coz-Bouhnik, M. (2005) Adsorption of
548 REE(III)-humate complexes onto MnO_2: experimental evidence for cerium anomaly and
549 lanthanide tetrad effect suppression. Geochimica et Cosmochimica Acta, 69, 4825-4835.

550 Fedo, C., Grant, G. and Nesbitt, H. (1997) Paleoclimatic control on the composition of the
551 Paleoproterozoic Serpent Formation, Huronian Supergroup, Canada: a greenhouse to icehouse
552 transition. Precambrian Research, 86, 201-223.

553 Hem, J.D. (1963) Chemical equilibria and rates of manganese oxidation, 71 p. United States
554 Government Printing Office, Washington.

555 Holland, H.D. (1984) The Chemical Evolution of the Atmosphere and Oceans, 598 p. Princeton
556 University Press, Princeton, N.J.

557 Ichimura, K. and Murakami, T. (2009) Formation of rare earth phosphate minerals in 2.45-Ga
558 paleosol. Journal of Mineralogical and Petrological Sciences, 104, 86-91.

559 Imai, N., Terashima, S., Itoh, S. and Ando, A. (1995) 1994 compilation of analytical data for
560 minor and trace elements in 17 GSJ geochemical reference samples: "Igneous Rock Series".
561 Geostandards Newsletter, 23, 135-213.

562 Imai, N., Terashima, S., Itoh, S. and Ando, A. (1999) 1998 compilation of analytical data for
563 five GSJ geochemical reference samples: The "Instrumental analysis series". Geostandards
564 Newsletter, 19, 223-250.

565 Janots, E., Bernier, F., Brunet, F., Munoz, M., Trcera, N., Berger, A. and Lanson, M. (2015)
566 Ce(III) and Ce(IV) (re)distribution and fractionation in a laterite profile from Madagascar:
567 Insights from in situ XANES spectroscopy at the Ce L-III-edge. Geochimica et Cosmochimica
568 Acta, 153, 134-148.

569 Jonasson, R.G. and Vance, E.R. (1986) DTA study of the rhabdophane to monazite
570 transformation in rare earth (La-Dy) phosphates. Thermochimica Acta, 108, 65-72.

571 Kogure, T. (2003) A program to assist Kikuchi pattern analyses. Journal of the Crystallographic
572 Society of Japan, 45, 391-395 (in Japanese).

573 Kon, Y., Murakami, H., Takagi, T. and Watanabe, Y. (2011) The development of whole rock
574 analysis of major and trace elements in XRF glass beads by fsLA-ICPMS in GSJ geochemical
575 reference samples. Geochemical Journal, 45, 387-416.

576 Liu, X., Wang, Q., Zhang, Q., Zhang, Y. and Li, Y. (2016) Genesis of REE minerals in the karstic
577 bauxite in western Guangxi, China, and its constraints on the deposit formation conditions. Ore
578 Geology Reviews, 75, 100-115.

579 Lottermoser, B.G. (1990) Rare-earth element mineralization within the Mt-Weld carbonatite
580 laterite, Western-Australia. Lithos, 24, 151-167.

581 Macfarlane, A.W., Danielson, A. and Holland, H.D. (1994) Geology and major and trace element
582 chemistry of late Archean weathering profiles in the Fortescue Group, Western Australia:
583 implications for atmospheric P_{O2}. Precambrian Research, 65, 297-317.

584 McDonough, W. and Sun, S. (1995) The composition of the Earth. Chemical Geology, 120,
585 223-253.

586 McNaught, A.D. and Wilkinson, A.D. (1997) Compendium of Chemical Terminology, 2nd ed.
587 (the "Gold Book") Blackwell Scientific Publications, Oxford.

588 Moffett, J.W. (1990) Microbially mediated Cerium oxidaiton in seawater. Nature, 345, 421-423.

589 Moffett, J.W. (1994) A radiotracer study of cerium and manganese uptake onto suspended
590 particles in Chesapeake Bay. Geochimica et Cosmochimica Acta, 58, 695-703.

591 Murakami, T., Utsunomiya, S., Imazu, Y. and Prasad, N. (2001) Direct evidence of late Archean
592 to early Proterozoic anoxic atmosphere from a product of 2.5 Ga old weathering. Earth and
593 Planetary Science Letters, 184, 523-528.

594 Murakami, T., Sreenivas, B., Das Sharma, S. and Sugimori, H. (2011) Quantification of
595 atmospheric oxygen levels during the Paleoproterozoic using paleosol compositions and iron
596 oxidation kinetics. Geochimica et Cosmochimica Acta, 75, 3982-4004.

597 Nagy, G., Draganits, E., Demeny, A., Panto, G. and Arkai, P. (2002) Genesis and
598 transformations of monazite, florencite and rhabdophane during medium grade
599 metamorphism: examples from the Sopron Hills, Eastern Alps. Chemical Geology, 191, 25-46.

600 Nakada, R., Takahashi, Y. and Tanimizu, M. (2013) Isotopic and speciation study on cerium
601 during its solid-water distribution with implication for Ce stable isotope as a paleo-redox proxy.
602 Geochimica et Cosmochimica Acta, 103, 49-62.

603 Nelson, C.S. and Cochrane, R.H. (1970) A rapid X-ray method for the quantitative
604 determination of selected minerals in fine-grained and altered rocks. Tane, 16, 151-162.

605 Nesbitt, H.W. (1979) Mobility and fractionation of rare-earth elements during weathering of a
606 granodiorite. Nature, 279, 206-210.

607 Nesbitt, H.W. and Young, G.M. (1982) Early Proterozoic climates and plate motions inferred
608 from major element chemistry of lutites. Nature, 299, 715-717.

609 Pan, Y.M. and Stauffer, M.R. (2000) Cerium anomaly and Th/U fractionation in the 1.85 Ga Flin
610 Flon Paleosol: Clues from REE- and U-rich accessory minerals and implications for
611 paleoatmospheric reconstruction. American Mineralogist, 85, 898-911.

612 Panahi, A., Young, G.M. and Rainbird, R.H. (2000) Behavior of major and trace elements
613 (including REE) during Paleoproterozoic pedogenesis and diagenetic alteration of an Archean
614 granite near Ville Marie, Québec, Canada. Geochimica et Cosmochimica Acta, 64, 2199-2220.

615 Range, K.J. and Range, A.W.A. (1969) Fire-clay type kaolinite or fire clay mineral?
616 Experimental classification of kaolinite-halloysite minerals. In L. Heller, Ed., Proceedings of the
617 International Clay Conference, Tokyo, 1969, ed. 1, p. 3-13. Israel Universities Press,
618 Jerusalem.

619 Rye, R. and Holland, H.D. (1998) Paleosols and the evolution of atmospheric oxygen: A critical
620 review. American Journal of Science, 298, 621-672.

621 Sanematsu, K., Kon, Y. and Imai, A. (2015) Influence of phosphate on mobility and adsorption
622 of REEs during weathering of granites in Thailand. Journal of Asian Earth Sciences, 111, 14-30.

623 Sawka, W.N., Banfield, J.F. and Chappell, B.W. (1986) A Weathering-Related Origin of
624 Widespread Monazite in S-Type Granites. Geochimica et Cosmochimica Acta, 50, 171-175.

625 Seredin, V.V. and Dai, S. (2012) Coal deposits as potential alternative sources for lanthanides
626 and yttrium. International Journal of Coal Geology, 94, 67-93.

627 Takahashi, Y., Shimizu, H., Kagi, H., Yoshida, H., Usui, A. and Nomura, M. (2000) A new
628 method for the determination of Ce^{III}/Ce^{IV} ratios in geological materials; application for
629 weathering, sedimentary and diagenetic processes. Earth and Planetary Science Letters, 182,
630 201-207.

631 Takahashi, Y., Manceau, A., Geoffroy, N., Marcus, M.A. and Usui, A. (2007) Chemical and
632 structural control of the partitioning of Co, Ce, and Pb in marine ferromanganese oxides.
633 Geochimica et Cosmochimica Acta, 71, 984-1008.

634 Taunton, A. E., Welch, S.A. and Banfield, J. F. (2000) Microbial controls on phosphate and
635 lanthanide distributions during granite weathering and soil formation. Chemical Geology, 169,
636 371-382

637 Taylor, S.R. and McLennan, S.M. (1988) The signifiance of the rare earth in geochemistry and
638 cosmochemistry. In K.A. Gschneidner and L. Eyring, Eds., Handbook of Physics and Chemistry
639 of Rare Earths, vol. 11, p. 485-578. Elsevier, Amsterdam.

640 Terashima, S., Taniguchi, M., Mikoshiba, M. and Imai, N. (1998) Preparation of two new GSJ
641 geochemical reference materials: Basalt JB-1b and coal fly ash JCFA-1. Geostandards
642 Newsletter-the Journal of Geostandards and Geoanalysis, 22, 113-117.

643 Utsunomiya, S., Murakami, T., Nakada, M. and Kasama, T. (2003) Iron oxidation state of a
644 2.45-Byr-old paleosol developed on mafic volcanics. Geochimica et Cosmochimica Acta, 67,
645 213-221.

646 Wiggering, H. and Beukes, N. (1990) Petrography and geochemistry of a 2000-2200-Ma-old
647 hematitic paleoalteration profile on Ongeluk basalt of the Transvaal Supergroup, Griqualand
648 West, South-Africa. Precambrian Research, 46, 241-258.

649 Williams, C.T. (1996) Analysis of rare earth minerals. In A.P. Jones, A.P. Wall and C.T. Williams,
650 Eds., Rare Earth Minerals, p. 327-348. Chapman and Hall, London.

651 Yang, W. and Holland, H. (2003) The Hekpoort paleosol profile in Strata 1 at Gaborone,
652 Botswana: Soil formation during the great oxidation event. American Journal of Science, 303,
653 187-220.

654 Yang, W., Holland, H. and Rye, R. (2002) Evidence for low or no oxygen in the late Archean
655 atmosphere from the similar to 2.76 Ga Mt. Roe #2 paleosol, Western Australia: Part 3.
656 Geochimica et Cosmochimica Acta, 66, 3707-3718.

657 Yu, C., Boily, J.-F., Shchukarev, A., Drake, H., Song, Z., Hogmalm, K.J., and Åström, M.E.
658 (2018) A cryogenic XPS study of Ce fixation on nanosized manganite and vernadite: Interfacial
659 reactions and effects of fulvic acid complexation. Chemical Geology, 483, 304-311.

660

661 Figure captions

662

663 Fig. 1. Modal composition and clay-mineral abundance changes with depth. The
664 locations of the samples are shown by arrows and sample names (an approximate depth
665 for sample YMK7). The upper soil was not sampled because it was mixed with plant
666 roots.

667

668 Fig. 2. Chemical changes with depth: chemical index of alteration (CIA: $\{Al_2O_3/(Al_2O_3$
669 $+ CaO + Na_2O + K_2O)\}\times 100$ (in moles)) (Nesbitt and Young 1982), loss on ignition
670 (LOI), concentrations of Na_2O and CaO, total concentrations of REEs, LREEs and
671 HREEs (ΣREE, ΣLREE and ΣHREE, respectively) and Ce anomaly ($Ce/Ce^* =$
672 $Ce_N/(La_N\times Pr_N)^{1/2}$; REE_N: REE concentration normalized by CI chondrite (McDonough
673 and Sun 1995)). Because expanded uncertainties at a coverage factor of 1 are smaller
674 than or similar to the symbol size, they are not given for simplicity.

675

676 Fig. 3. X-ray diffraction patterns of oriented < 2 μm fraction of sample YMK2 after (a)
677 air-drying, (b) hydrazine treatment, (c) washing the hydrazine-treated specimen by
678 water, (d) glycerol treatment of the hydrazine/water-treated specimen, and (e) heating at
679 500˚C for 1 h. See text for the details.

680

681 Fig. 4. Rare earth patterns of the bulk samples normalized by (a) CI chondrite
682 (McDonough and Sun 1995) and (b) parent rock (sample YMK7). In Fig. 4a, because
683 expanded uncertainties at a coverage factor of 1 are smaller than or similar to the
684 symbol size, they are not given for simplicity; in Fig. 4b, uncertainty bars represent
685 expanded uncertainties at a coverage factor of 1.

686

687 Fig. 5. Backscattered electron images showing occurrences of cerianite-(Ce) and the
688 four species of rhabdophanes. (a) Rhabdophane-(La) and -(Ce) and cerianite-(Ce) in
689 sample YMK4. (b) and (c) Magnified images, in Fig. 5a, of cerianite-(Ce) in veins
690 accompanied by Mn (oxyhydr)oxide and rhabdophane-(La) and -(Ce) occurring as
691 aggregates of fine crystals, respectively. (d) Rhabdophane-(La) in veins, usually in
692 contact with kaolin, in sample YMK2. (e) Rhabdophane-(Ce) in a grain boundary

693 between orthoclase grains in sample YMK4. (f) Rhabdophane-(La) and -(Nd) in veins in
694 plagioclase mostly filled with kaolin in sample YMK2. (g) Rhabdophane-(Nd) in
695 smectite and associated with fluorapatite in sample YMK6. (h) Rhabdophane-(Y) in
696 smectite and accompanied by fluorapatite in sample YMK6. (i) Electron backscatter
697 diffraction pattern of rhabdophane-(Ce) in Fig. 5e, and (j) a corresponding calculated
698 pattern. Rhb-Y, rhabdophane-(Y), Rhb-La, rhabdophane-(La); Rhb-Ce,
699 rhabdophane-(Ce), Rhb-Nd, rhabdophane-(Nd); Cer, cerianite-(Ce); Mn-ox, Mn
700 (oxyhydr)oxide; Pl, plagioclase; Or, orthoclase; Bt, biotite; Kl, kaolin; Sme, smectite;
701 Ap, fluorapatite. The kaolin minerals in Fig. 5 are probably halloysite.
702
703 Fig. 6. Rare earth patterns of average chemical compositions of (a) primary
704 REE-bearing minerals normalized by CI chondrite (McDonough and Sun 1995) and (b)
705 secondary rhabdophane normalized by CI chondrite and further normalized by La (scale
706 of the left vertical axis). The REE pattern of the parent rock (sample YMK7; scale of the
707 right vertical axis) and those of allanite-(Ce) of the parent rock and bulk sample YMK2
708 are added to Figs. 6a and 6b, respectively, for comparison. See text for the calculation of
709 the average chemical compositions. Because the LREE patterns of samples YMK2 to
710 YMK 6 are similar (Fig. 4a), the REE pattern of only sample YMK2 is given in Fig. 6b

711 to avoid complicated drawing. Some of the lines are unconnected because the
712 concentrations of the related REEs are under detection limits. Uncertainty bars represent
713 expanded uncertainties at a coverage factor of 1 in Fig. 6a and for allanite-(Ce) in Fig.
714 6b, and concentration dispersions of one standard deviation for secondary rhabdophane
715 in Fig. 6b.
716
717 Fig. 7. REEs fractional contributions of primary REE-bearing minerals to corresponding
718 REEs of the parent rock. Data points not shown in the figure are data not detected or
719 under quantitative detection limits. See text for the calculation of the REE fractional
720 contributions of primary REE-bearing minerals. Uncertainty bars represent expanded
721 uncertainties at a coverage factor of 1.
722
723 Fig. 8. (a) Ratios of individual REEs between rhabdophane and allanite-(Ce), and
724 variations of (b) Ce/Ce^{*} values of rhabdophane-(La), -(Ce), -(Nd) and -(Y) particles and
725 (c) Nd/La ratios of rhabdophane-(La), -(Ce) and -(Nd) particles. A data point in Fig. 8a
726 is obtained as follows: A ratio of ΣREE of allanite-(Ce) to that of rhabdophane (i.e.,
727 ratio of $\Sigma C_{n,REE}$ between the two minerals) is calculated first, a $C_{n,REE}$ value of the
728 rhabdophane is multiplied by the ratio of ΣREE, and then the obtained value is divided

729 by a $C_{n,REE}$ value of allanite-(Ce), and log(the final value) is plotted in the figure. See
730 equation (1) to calculate a $C_{n,Z}$ value; $C_{n,REE}$ is $C_{n,Z}$ where Z is an REE. See the caption
731 of Fig. 1 for Ce/Ce*. Nd and La in Fig. 8c are the concentrations (wt%) of respective
732 elements. The data from weathered rocks, i.e., samples YMK2 and YMK4 (Fig. 1 and
733 Table 5) were used for the data points in Fig. 8c. The Nd/La ratios of rhabdophane-(Y)
734 are not given in Fig. 8c because its formation mechanisms are likely to be different from
735 those of the other types of rhabdophane (see the Discussion section). In Fig. 8a, bars
736 represent uncertainties of concentration dispersions of one standard deviation of
737 rhabdophane and if not given, the uncertainties are smaller than the symbol size; and in
738 Figs. 8b and 8c, they are not given for simplicity because the uncertainties are smaller
739 than or similar to the symbol size.
740
741 Fig. 9. Schematic drawing of LREE redistributions between secondary minerals and Ce
742 anomalies in bulk weathered layers during oxic weathering (see text for the three cases).
743 We only show one or two weathered layers of one weathering profile for simplicity. +,
744 positive anomaly; −, negative anomaly; 0, no anomaly.
745
746

747

This is a preprint, the final version is subject to change, of the American Mineralogist (MSA)
Cite as Authors (Year) Title. American Mineralogist, in press.
DOI: https://doi.org/10.2138/am-2020-7148

Table 1. Chemical compositions and informations of the bulk samples (wt% for major elements and mg/kg for trace elements).[a]

Sample	YMK1	YMK2	YMK3	YMK4	YMK5	YMK6	YMK7
Depth	5.0 m	10.4 m	19.2 m	25.0 m	29.0 m	31.0 m	Parent rock
SiO_2 (wt%)	73.59 ±0.03	73.60 ±0.03	74.72 ±0.03	74.21 ±0.03	74.69 ±0.03	74.64 ±0.03	72.73 ±0.03
TiO_2	0.16 ±0.00	0.17 ±0.00	0.14 ±0.00	0.15 ±0.00	0.12 ±0.00	0.12 ±0.00	0.19 ±0.00
Al_2O_3	14.45 ±0.03	14.62 ±0.03	13.90 ±0.03	13.40 ±0.02	13.26 ±0.02	13.29 ±0.02	13.96 ±0.03
Fe_2O_3[b]	1.65 ±0.00	1.88 ±0.00	1.55 ±0.00	1.73 ±0.00	1.46 ±0.00	1.50 ±0.00	1.97 ±0.00
MnO	0.02 ±0.00	0.03 ±0.00	0.02 ±0.00	0.03 ±0.00	0.03 ±0.00	0.03 ±0.00	0.03 ±0.00
MgO	0.16 ±0.00	0.16 ±0.00	0.13 ±0.00	0.16 ±0.00	0.12 ±0.00	0.13 ±0.00	0.24 ±0.00
CaO	0.67 ±0.00	0.97 ±0.01	1.47 ±0.01	1.19 ±0.01	1.54 ±0.01	1.48 ±0.01	2.16 ±0.01
Na_2O	1.63 ±0.01	2.25 ±0.01	3.05 ±0.01	2.57 ±0.01	3.05 ±0.01	3.09 ±0.01	3.27 ±0.01
K_2O	4.50 ±0.01	4.64 ±0.01	4.46 ±0.01	4.58 ±0.01	4.66 ±0.01	4.71 ±0.01	4.14 ±0.01
P_2O_5	0.013 ±0.001	0.016 ±0.001	0.017 ±0.001	0.019 ±0.001	0.025 ±0.001	0.021 ±0.001	0.038 ±0.002
LOI[c]	2.91 ±0.29	2.25 ±0.23	0.96 ±0.10	1.33 ±0.13	0.36 ±0.04	0.38 ±0.04	0.41 ±0.04
Total	99.75 ±0.05	100.60 ±0.05	100.43 ±0.05	99.36 ±0.05	99.31 ±0.05	99.38 ±0.05	99.14 ±0.05
CIA (%)[d]	62.2 ±0.0	58.2 ±0.0	52.6 ±0.0	54.2 ±0.0	50.8 ±0.0	50.8 ±0.0	50.3 ±0.0
Sc (mg/kg)	3.5 ±0.1	3.7 ±0.1	2.8 ±0.1	3.3 ±0.0	2.4 ±0.0	1.9 ±0.0	5.8 ±0.1
Ga	24.5 ±0.7	26.8 ±0.4	25.6 ±0.5	25.0 ±0.8	25.4 ±0.8	23.5 ±0.3	29.6 ±0.7
Rb	139 ±9	147 ±9	134 ±8	141 ±5	133 ±5	134 ±8	129 ±5
Sr	121 ±3	151 ±6	176 ±4	171 ±5	193 ±6	187 ±7	220 ±5
Y	12.6 ±0.6	17.8 ±0.6	14.9 ±0.5	18.5 ±0.9	14.2 ±0.7	15.5 ±1.0	20.9 ±0.7
Zr	127 ±5	154 ±7	138 ±7	124 ±3	114 ±5	138 ±7	163 ±6
Nb	5.9 ±0.2	6.8 ±0.4	5.3 ±0.2	6.3 ±0.2	5.0 ±0.2	4.8 ±0.2	6.8 ±0.3
Cs	2.7 ±0.2	3.5 ±0.1	3.1 ±0.2	3.0 ±0.1	2.4 ±0.1	2.5 ±0.1	2.8 ±0.2
Ba	1,156 ±27	1,253 ±48	1,316 ±74	1,248 ±51	1,388 ±48	1,262 ±60	1,472 ±31
La	28.4 ±1.5	42.0 ±2.4	45.3 ±2.3	38.0 ±2.1	42.6 ±1.5	39.9 ±2.4	37.3 ±1.9
Ce	98.6 ±2.9	94.2 ±5.5	89.8 ±6.5	88.8 ±4.3	89.5 ±4.3	86.0 ±5.6	77.0 ±2.9
Pr	6.7 ±0.3	9.5 ±0.5	10.2 ±0.7	9.1 ±0.5	9.5 ±0.5	9.2 ±0.5	8.3 ±0.3
Nd	24.8 ±1.1	33.8 ±1.8	37.5 ±1.8	31.9 ±1.6	33.8 ±0.8	33.1 ±1.7	30.1 ±1.8
Sm	4.0 ±0.4	5.3 ±0.4	5.3 ±0.5	5.1 ±0.3	5.1 ±0.1	5.3 ±0.3	4.9 ±0.4
Eu	0.78 ±0.05	0.84 ±0.04	0.90 ±0.07	0.87 ±0.05	0.88 ±0.03	0.85 ±0.06	1.02 ±0.04
Gd	3.2 ±0.3	4.3 ±0.1	4.0 ±0.2	4.2 ±0.2	3.8 ±0.2	4.0 ±0.2	4.1 ±0.1
Tb	0.41 ±0.04	0.55 ±0.05	0.51 ±0.05	0.60 ±0.03	0.53 ±0.02	0.52 ±0.02	0.62 ±0.04
Dy	2.5 ±0.1	3.4 ±0.2	3.0 ±0.2	3.4 ±0.2	3.0 ±0.2	3.0 ±0.2	3.8 ±0.2
Ho	0.50 0.02	0.68 0.04	0.58 0.02	0.70 0.04	0.58 0.03	0.62 0.06	0.77 0.04
Er	1.3 ±0.1	1.8 ±0.1	1.7 ±0.1	2.0 ±0.0	1.7 ±0.1	1.8 ±0.2	2.3 ±0.1
Tm	0.19 ±0.02	0.29 ±0.03	0.24 ±0.01	0.30 ±0.02	0.23 ±0.02	0.25 ±0.03	0.31 ±0.02
Yb	1.5 ±0.1	2.1 ±0.1	1.8 ±0.1	2.0 ±0.3	1.8 ±0.1	1.9 ±0.1	2.3 ±0.1
Lu	0.22 ±0.01	0.30 ±0.03	0.27 ±0.02	0.31 ±0.03	0.27 ±0.02	0.27 ±0.02	0.33 ±0.02
Hf	3.9 ±0.4	4.5 ±0.4	4.1 ±0.3	4.0 ±0.3	3.8 ±0.2	4.2 ±0.3	4.5 ±0.3
Ta	0.45 ±0.02	0.57 ±0.06	0.49 ±0.05	0.51 ±0.04	0.42 ±0.01	0.43 ±0.03	0.56 ±0.05
Th	12.2 ±0.8	16.4 ±1.5	13.2 ±1.2	11.8 ±1.1	14.1 ±1.0	13.9 ±1.3	11.3 ±0.7
U	1.3 ±0.1	1.8 ±0.2	1.1 ±0.1	1.7 ±0.2	1.5 ±0.1	1.6 ±0.1	1.5 ±0.1
ΣREE[e]	189.1 ±3.5	220.5 ±6.3	218.7 ±7.2	209.0 ±5.1	209.9 ±4.7	203.9 ±6.4	199.9 ±4.0
ΣLREE[e]	163.2 ±3.5	185.7 ±6.3	189.0 ±7.2	173.8 ±5.0	181.4 ±4.7	174.3 ±6.3	158.7 ±3.9
ΣHREE[e]	9.8 ±0.3	13.3 ±0.3	12.1 ±0.3	13.5 ±0.4	11.9 ±0.3	12.3 ±0.4	14.5 ±0.2
Ce/Ce^* [f]	1.73 ±0.08	1.14 ±0.08	1.01 ±0.08	1.16 ±0.07	1.08 ±0.06	1.08 ±0.08	1.06 ±0.05
Eu/Eu^* [f]	0.68 ±0.07	0.54 ±0.03	0.59 ±0.06	0.57 ±0.04	0.60 ±0.03	0.56 ±0.04	0.69 ±0.04

[a]Expanded uncertainties at a coverage factor of 1.

[b]Total iron as Fe_2O_3.

[c]LOI: loss on ignition. We assumed an uncertainty of 10 % (e.g., Braun et al. 1998).

[d]CIA: chemical index of alteration $\{Al_2O_3/(Al_2O_3 + CaO + Na_2O + K_2O)\}$x100 (in moles) (Nesbitt and Young 1982).

[e]ΣREE: total rare earth elements; ΣLREE: total light rare earth elements; and ΣHREE: total heavy rare earth elements.

[f]$Ce/Ce^* = Ce_N/(La_N x Pr_N)^{1/2}$ and $Eu/Eu^* = Eu_N/(Sm_N x Gd_N)^{1/2}$ (REE_N: REE concentration normalized by CI chondrite (McDonough and Sun 1995)).

This is a preprint, the final version is subject to change, of the American Mineralogist (MSA)
Cite as Authors (Year) Title. American Mineralogist, in press.
DOI: https://doi.org/10.2138/am-2020-7148

Table 2. List of REE-bearing minerals.

	Mineral	Ideal formula
Primary minerals	Allanite-(Ce)	$(Ca,Ce)_2(Al_2Fe^{2+})[Si_2O_7][SiO_4]O(OH)$
	Allanite-(Y)	$(Ca,Y)_2(Al_2Fe^{2+})[Si_2O_7][SiO_4]O(OH)$
	Epidote	$Ca_2(Al_2Fe^{2+})[Si_2O_7][SiO_4]O(OH)$
	Fluorapatite	$Ca_5(PO_4)_3F$
	Ca- and Y-rich unidentified phase	Unknown
	Hornblende	$Ca_2(Fe,Mg,Al)_5(Al,Si)_8O_{22}(OH)_2$
	Titanite	$CaTiSiO_5$
	Xenotime-(Y)	YPO_4
	Zircon	$ZrSiO_4$
Secondary minerals	Cerianite-(Ce)	CeO_2
	Rhabdophane-(La)	$La(PO_4) \cdot H_2O$
	Rhabdophane-(Ce)	$Ce(PO_4) \cdot H_2O$
	Rhabdophane-(Nd)	$Nd(PO_4) \cdot H_2O$
	Rhabdophane-(Y)	$Y(PO_4) \cdot H_2O$
	Y-rich unidentified phase	Unknown

Table 3. Average compositions (wt%) and chemical informations of primary REE-bearing minerals.[a]

	Allanite-(Ce)	Allanite-(Y)	Epidote	Xenotime-(Y)	Fluorapatite	Zircon	Ca- and Y-rich unidentified phase	Titanite	Hornblende
No. of samples	35	6	5	3	10	11	3	3	3
B_2O_3	N.A.[b]	N.A.	N.A.	N.A.	N.A.	N.A.	15.0 ±4.3	N.A.	N.A.
Na_2O	< 0.03	< 0.03	< 0.03	< 0.03	< 0.03	< 0.03	< 0.03	< 0.03	1.65 ±0.03
MgO	0.47 ±0.09	< 0.02	< 0.02	0.04 ±0.07	< 0.02	< 0.02	< 0.02	0.17 ±0.08	3.63 ±0.11
Al_2O_3	15.72 ±0.10	21.29 ±0.27	25.53 ±0.37	0.29 ±0.49	0.04 ±0.02	< 0.02	4.48 ±0.34	5.97 ±0.73	8.83 ±0.12
SiO2	32.61 ±0.14	34.38 ±0.17	37.17 ±0.20	6.75 ±5.46	0.68 ±0.08	34.19 ±0.13	23.13 ±1.21	30.61 ±0.19	42.31 ±0.08
P_2O_5	< 0.06	< 0.06	< 0.06	26.29 ±4.79	39.76 ±0.28	0.09 ±0.03	< 0.06	< 0.06	< 0.06
SO_3	< 0.2	< 0.2	< 0.2	< 0.2	< 0.2	< 0.2	< 0.2	< 0.2	< 0.2
K_2O	< 0.02	< 0.02	< 0.02	0.08 ±0.07	0.09 ±0.02	< 0.02	0.15 ±0.06	0.14 ±0.07	0.65 ±0.01
CaO	10.42 ±0.06	13.89 ±0.11	21.93 ±0.74	0.53 ±0.85	54.08 ±0.17	< 0.02	16.12 ±0.49	26.05 ±0.70	10.44 ±0.10
TiO_2	1.42 ±0.08	0.17 ±0.06	< 0.11	< 0.11	< 0.11	< 0.11	< 0.14 ±0.05	26.97 ±1.38	0.98 ±0.04
V_2O_3	0.04 ±0.01	< 0.02 ±0.01	< 0.02 ±0.01	< 0.02	< 0.02	< 0.02	< 0.02	< 0.02	0.03 ±0.00
Cr_2O_3	< 0.02	< 0.02	< 0.02	< 0.02	< 0.02	< 0.02	< 0.02	< 0.02	< 0.02
MnO	0.27 ±0.01	0.64 ±0.02	0.29 ±0.04	< 0.02	0.08 ±0.00	< 0.02	0.91 ±0.19	0.11 ±0.01	0.95 ±0.03
FeO	14.28 ±0.06	11.62 ±0.23	8.18 ±0.35	1.61 ±1.57	0.45 ±0.02	0.37 ±0.02	0.93 ±0.21	1.21 ±0.12	27.74 ±0.10
NiO	< 0.03	< 0.03	< 0.03	< 0.03	< 0.03	< 0.03	< 0.03	< 0.03	< 0.03
SrO	< 0.08	< 0.08	< 0.08	< 0.08	< 0.08	< 0.08	< 0.08	< 0.08	< 0.08
Y_2O_3	0.34 ±0.04	8.32 ±0.50	1.23 ±0.46	41.06 ±5.78	0.67 ±0.08	< 0.06	24.87 ±2.68	2.87 ±0.82	0.21 ±0.04
ZrO_2	< 0.13	< 0.13	< 0.13	< 0.13	< 0.13	62.51	< 0.13	< 0.13	< 0.13
La_2O_3	5.47 ±0.13	0.23 ±0.09	< 0.14	< 0.14	< 0.14	< 0.14	< 0.14	< 0.14	< 0.14
Ce_2O_3	10.94 ±0.15	0.87 ±0.24	0.22 ±0.11	0.33 ±0.57	0.15 ±0.05	< 0.15	< 0.15	< 0.15	< 0.15
Pr_2O_3	1.16 ±0.04	0.19 ±0.05	< 0.07	< 0.07	< 0.07	< 0.07	< 0.07	< 0.07	< 0.07
Nd_2O_3	4.16 ±0.08	1.01 ±0.23	0.24 ±0.11	0.34 ±0.34	0.17 ±0.02	< 0.12	< 0.12	< 0.12	< 0.12
Sm_2O_3	0.55 ±0.02	0.55 ±0.08	0.13 ±0.06	0.84 ±0.15	< 0.08	< 0.08	0.31 ±0.08	0.09 ±0.03	< 0.08
Eu_2O_3	< 0.04	< 0.04	< 0.04	< 0.04	< 0.04	< 0.04	< 0.04	< 0.04	< 0.04
Gd_2O_3	0.28 ±0.07	1.08 ±0.06	0.24 ±0.10	1.69 ±0.46	0.12 ±0.05	< 0.08	0.72 ±0.22	0.23 ±0.08	< 0.08
Tb_2O_3	< 0.08	< 0.08	< 0.08	0.36 ±0.10	< 0.08	< 0.08	< 0.18 ±0.04	< 0.08	< 0.08
Dy_2O_3	0.11 ±0.01	1.32 ±0.05	0.23 ±0.09	4.23 ±0.73	0.11 ±0.01	0.04 ±0.01	2.99 ±0.09	0.41 ±0.13	< 0.04
Ho_2O_3	< 0.09	0.20 ±0.02	< 0.09	1.26 ±0.13	< 0.09	< 0.09	0.93 ±0.07	< 0.09	< 0.09
Er_2O_3	< 0.05	0.85 ±0.06	0.11 ±0.04	3.61 ±0.47	0.06 ±0.01	< 0.05	2.60 ±0.34	0.30 ±0.09	< 0.05
Tm2O3	< 0.05	0.13 ±0.01	< 0.05	0.55 ±0.13	< 0.05	< 0.05	0.41 ±0.08	< 0.07	< 0.05
Yb_2O_3	< 0.05	0.64 ±0.05	0.07 ±0.03	4.32 ±1.37	< 0.05	0.07 ±0.02	3.13 ±0.62	0.29 ±0.07	< 0.05
Lu_2O_3	< 0.11	< 0.11	< 0.11	0.57 ±0.22	< 0.11	< 0.11	0.45 ±0.11	< 0.11	< 0.11
HfO_2	N.A.	N.A.	N.A.	N.A.	N.A.	N.A.	N.A.	N.A.	N.A.
PbO	< 0.03	< 0.03	< 0.03	0.72 ±0.22	< 0.03	< 0.03	< 0.03	< 0.03	< 0.03
ThO_2	1.22 ±0.06	0.66 ±0.19	0.19 ±0.08	0.85 ±1.13	< 0.06	< 0.06	< 0.06	< 0.06	< 0.06
UO_2	< 0.06	< 0.06	< 0.06	2.10 ±0.91	< 0.06	0.22 ±0.06	< 0.06	< 0.06	< 0.06
F	< 0.7	< 0.7	< 0.7	< 0.7	3.10 ±0.33	< 0.7	< 0.7	1.64 ±0.36	< 0.7
$-O(=F_2)$					1.31			0.69 ±0.15	
Cl	< 0.02	< 0.02	< 0.02	< 0.02	< 0.02	< 0.02	< 0.02	< 0.02	0.02 ±0.00
$-O(=Cl_2)$									0.00 ±0.00
Total [c]	99.4 ±0.4	98.1 ±0.3	95.8 ±0.4	98.4 ±0.4	98.3 ±0.4	97.5 ±0.4	97.5 ±0.3	96.5 ±0.3	97.4 ±0.3
ΣREE	19.6 ±0.2	12.7 ±0.5	2.0 ±0.4	47.3 ±4.8	1.0 ±0.1	0.1 ±0.0	29.3 ±2.2	3.3 ±0.7	0.2 ±0.0
$(Ce/Ce^*)_{CN}$	1.05 ±0.03	1.00 ±0.38	N.A.	N.A.	N.D.	N.D.	N.D.	N.D.	N.D.
$(Eu/Eu^*)_{CN}$	< 0.31	< 0.16	< 0.71	< 0.10	N.D.	N.D.	N.D.	N.D.	N.D.
Mod. com. ($x10^4$)[d]	809 ±215	108 ±29	6 ±5	Trace	896 ±47	328 ±24	2 ±2	27 ±14	1114 ±965

[a]Compositions by EMPA. Expanded uncertainties at a coverage factor of 1. Values of allanite-(Ce), allanite-(Y), epidote, fluorapatite, and zircon are weighed by the analyzed areas to correct systematic errors induced by the compositional heterogeneity.

[b]N.A.: not analyzed.

[c]Total adjusted for F and Cl in place of O.

[d]Mod. com.: modal composition of a mineral in the parent rock (wt%; see text for the details).

This is a preprint, the final version is subject to change, of the American Mineralogist (MSA)
Cite as Authors (Year) Title. American Mineralogist, in press.
DOI: https://doi.org/10.2138/am-2020-7148

Table 4. Average Compositions (wt%) and chemical informations of secondary REE-bearing minerals.[a]

	Rhabdophane-(La)		Rhabdophane-(Ce)		Rhabdophane-(Nd)		Rhabdophane-(Y)		Cerianite-(Ce)		Y-rich unidentified phase	
No. of samples	10		6		12		4		3		8	
Na_2O	< 0.03		< 0.03		0.41	(0.0 - 3.0)	< 0.03		< 0.06		< 0.45	
MgO	< 0.03		< 0.02		< 0.04	(< 0.01 - 0.06)	< 0.02		< 0.04		< 0.02	
Al_2O_3	0.56	(0.1 - 1.0)	0.77	(< 0.1 - 3.4)	2.27	(0.1- 4.4)	1.75	(0.7 - 2.9)	4.07	(2.9 - 5.3)	4.40	(1.1 - 7.7)
SiO_2	0.74	(0.3 - 1.2)	1.05	(< 0.07 - 3.4)	4.54	(0.7 - 8.4)	5.52	(0.3 - 10.8)	4.95	(2.4 - 7.5)	15.27	(7.0 - 23.6)
P_2O_5	29.01	(28.2 - 29.9)	30.47	(28.2 - 32.7)	25.79	(23.7 - 27.9)	24.28	(23.5 - 25.0)	4.88	(4.2 - 5.5)	15.91	(11.5 - 20.3)
SO_3	< 0.2		< 0.2		< 0.2		< 0.2		< 0.2		< 0.2	
K_2O	0.04	(< 0.02 - 0.07)	0.08	(0.06 - 0.10)	0.19	(< 0.02 - 0.7)	< 0.03		< 0.07		0.04	(0.02 - 0.06)
CaO	3.05	(2.5 - 3.6)	3.48	(2.9 - 4.1)	4.85	(< 0.02 - 12.2)	7.43	(4.2 - 10.7)	1.46	(0.8 - 2.1)	1.69	(0.4 - 3.0)
TiO2	< 0.11		< 0.11		< 0.11		0.12	(< 0.08 - 0.15)	N.A.[b]		< 0.11	
V_2O_3	0.03	(0.02 - 0.04)	< 0.02		0.04	(< 0.02 - 0.07)	0.02	(0.02 - 0.03)	N.A.		0.69	(0.2 - 1.2)
Cr_2O_3	< 0.02		< 0.02		< 0.02		< 0.02		N.A.		< 0.02	
MnO	0.08	(0.0 - 0.5)	0.10	(0.1 - 0.1)	< 0.04		< 0.05		2.80	(2.1 - 3.5)	0.15	(0.0 - 0.4)
FeO	0.27	(0.0 - 0.7)	0.24	(0.2 - 0.3)	1.47	(0.0 - 4.1)	4.40	(3.3 - 5.5)	0.82	(0.5 - 1.2)	2.04	(0.0 - 5.0)
NiO	< 0.03		< 0.03		< 0.03		< 0.03		N.A.		< 0.03	
SrO	< 0.08		< 0.08		< 0.08		< 0.08		N.A.		< 0.08	
Y_2O_3	3.95	(3.2 - 4.7)	3.36	(2.6 - 4.2)	5.07	(3.4 - 6.8)	9.52	(6.1 - 13.0)	< 0.28		24.82	(18.3 - 31.4)
ZrO_2	< 0.13		< 0.13		< 0.13		< 0.13		< 0.13		0.16	(< 0.13 - 0.3)
La_2O_3	18.61	(16.2 - 21.0)	14.24	(12.2 - 16.3)	13.63	(7.8 - 19.5)	5.30	(4.2 - 6.5)	0.29	(0.3 - 0.3)	0.23	(0.2 - 0.3)
Ce_2O_3	7.26	(2.6 - 11.9)	18.14	(10.6 - 25.7)	1.87	(0.6 - 3.1)	0.65	(0.4 - 0.9)	64.22	(52.1 - 76.4)	5.56	(< 0.1 - 11.3)
Pr_2O_3	5.09	(4.4 - 5.8)	3.62	(2.9 - 4.4)	4.06	(2.6 - 5.5)	2.23	(1.8 - 2.7)	< 0.25		0.21	(0.2 - 0.3)
Nd_2O_3	18.14	(16.0 - 20.2)	13.24	(10.3 - 16.2)	15.96	(11.0 - 20.9)	9.86	(7.7 - 12.1)	0.36	(0.2 - 0.5)	1.46	(1.0 - 1.9)
Sm_2O_3	3.15	(2.7 - 3.6)	2.22	(1.5 - 2.9)	3.22	(2.3 - 4.1)	3.03	(2.5 - 3.6)	< 0.14		1.01	(0.8 - 1.2)
Eu_2O_3	0.11	(0.06 - 0.16)	< 0.04		0.14	(0.1 - 0.2)	0.15	(0.1 - 0.2)	< 0.04		0.06	(0.04 - 0.08)
Gd_2O_3	1.81	(1.6 - 2.1)	1.34	(0.9 - 1.8)	2.10	(1.5 - 2.8)	2.74	(2.5 - 3.0)	< 0.14		2.21	(1.8 - 2.6)
Tb_2O_3	< 0.08		< 0.08		< 0.08		N.A.		< 0.08		0.29	(0.2 - 0.3)
Dy_2O_3	1.07	(0.9 - 1.3)	0.79	(0.6 - 1.0)	1.27	(0.85 - 1.69)	2.08	(1.7 - 2.5)	< 0.14		3.28	(2.5 - 4.1)
Ho_2O_3	< 0.09		< 0.09		0.09	(0.02 - 0.16)	N.A.		< 0.09		0.57	(0.4 - 0.7)
Er_2O_3	0.39	(0.32 - 0.46)	0.31	(0.2 - 0.4)	0.88	(0.0 - 2.3)	0.87	(0.5 - 1.2)	< 0.03		2.17	(1.6 - 2.8)
Tm_2O_3	< 0.05		< 0.05		< 0.05		< 0.15		< 0.05		0.26	(0.2 - 0.4)
Yb_2O_3	0.22	(0.2 - 0.3)	0.21	(0.2 - 0.3)	0.25	(0.2 - 0.3)	0.58	(0.2 - 1.0)	< 0.03		1.84	(1.1 - 2.6)
Lu_2O_3	< 0.11		< 0.11		< 0.11		< 0.11		< 0.11		0.18	(0.1 - 0.2)
PbO	< 0.03		< 0.03		< 0.03		< 0.14		< 0.04		< 0.03	
ThO_2	< 0.06		< 0.06		2.94	(< 0.1 - 7.9)	13.78	(9.2 - 18.4)	< 0.06		10.71	(< 0.1 - 23.8)
UO_2	< 0.06		0.25	(0.2 - 0.3)	0.64	(< 0.1 - 1.4)	< 0.23		< 0.04		0.29	(< 0.0 - 0.5)
Total	94.1	(92.0 - 96.3)	94.2	(90.0 - 98.4)	92.1	(86.2 - 98.1)	95.2	(89.7 - 100.7)	83.8	(76.0 - 91.5)	96.1	(91.8 - 100.4)
ΣREE	50.9	(46.0 - 55.8)	48.9	(41.6 - 56.2)	41.2	(34.0 - 48.3)	31.4	(27.8 - 35.0)	55.4	(45.0 - 65.8)	36.1	(28.9 - 43.3)
$(Ce/Ce^*)_{CN}$	0.20	(0.05 - 0.34)	0.62	(0.50 - 0.73)	0.06	(0.03 - 0.09)	0.04	(0.03 - 0.06)	> 57.4		< 18	
$(Eu/Eu^*)_{CN}$	0.13	(0.08 - 0.18)	< 0.17		0.18	(0.11 - 0.25)	0.16	(0.11 - 0.20)	N.A.		< 0.33	

[a]Compositions by EMPA. Concentration dispersions of one standard deviation are given in parentheses.

[b]N.A.: not analyzed.

This is a preprint, the final version is subject to change, of the American Mineralogist (MSA)
Cite as Authors (Year) Title. American Mineralogist, in press.
DOI: https://doi.org/10.2138/am-2020-7148

Table 5. REE-bearing mineral abundances.[a]

Sample (depth)	Aln-Ce	Aln-Y	Ep	FAp	Hbl	Ttn	Xen	Zrn	CaY-u	Cer	Rhb-La	Rhb-Ce	Rhb-Nd	Rhb-Y	Y-u
YMK1 (5.0 m)	-			-			-	++		++	-	-	-		
YMK2 (10.4 m)	-			-				++		++	++	++	++		
YMK3 (19.2 m)	++			-			-	++		+	+	+	+		
YMK4 (25.0 m)	+			-	-			++		++	++	++	++		
YMK5 (29.0 m)	++			+	+	-	-	++		-					-
YMK6 (31.0 m)	++			+	+	-		++	-	-			-	-	
YMK7 (PR[b])	++	+	-	++	++	-	-	++	-						

[a] The abundances of REE-bearing minerals were qualitatively estimated by their areas on backscattered electron micrographs.
++, common; +, minor; -, trace; blank, not found.
Aln-Ce, allanite-(Ce); Aln-Y, allanite-(Y); Ep, Epidote; FAp, Fluorapatite; Hbl, hornblende; Ttn, titanite; Xen, xenotime-(Y); Zrn, zircon; CaY-u, Ca- and Y-rich unidentified phase; Cer, cerianite-(Ce); Rhb-La, rhabdophane-(La); Rhb-Ce, rhabdophane-(Ce); Rhb-Nd, rhabdphane-(Nd); Rhb-Y, rhabdophane-(Y). ; Y-u, Y-rich unidentified phase

[b] PR, parent rock.

This is a preprint, the final version is subject to change, of the American Mineralogist (MSA)
Cite as Authors (Year) Title. American Mineralogist, in press.
DOI: https://doi.org/10.2138/am-2020-7148

Fig. 1

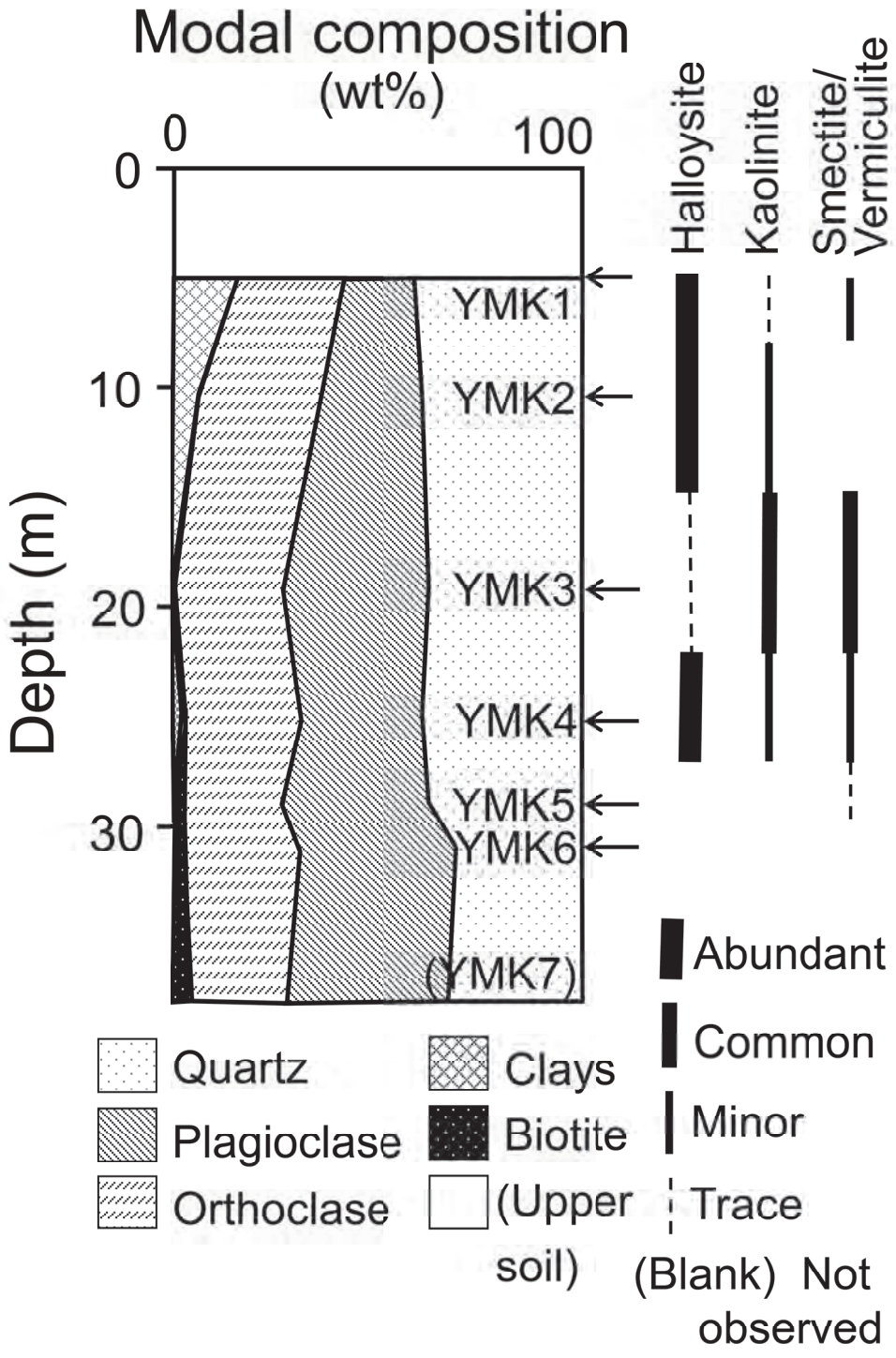

This is a preprint, the final version is subject to change, of the American Mineralogist (MSA)
Cite as Authors (Year) Title. American Mineralogist, in press.
DOI: https://doi.org/10.2138/am-2020-7148

Fig. 2

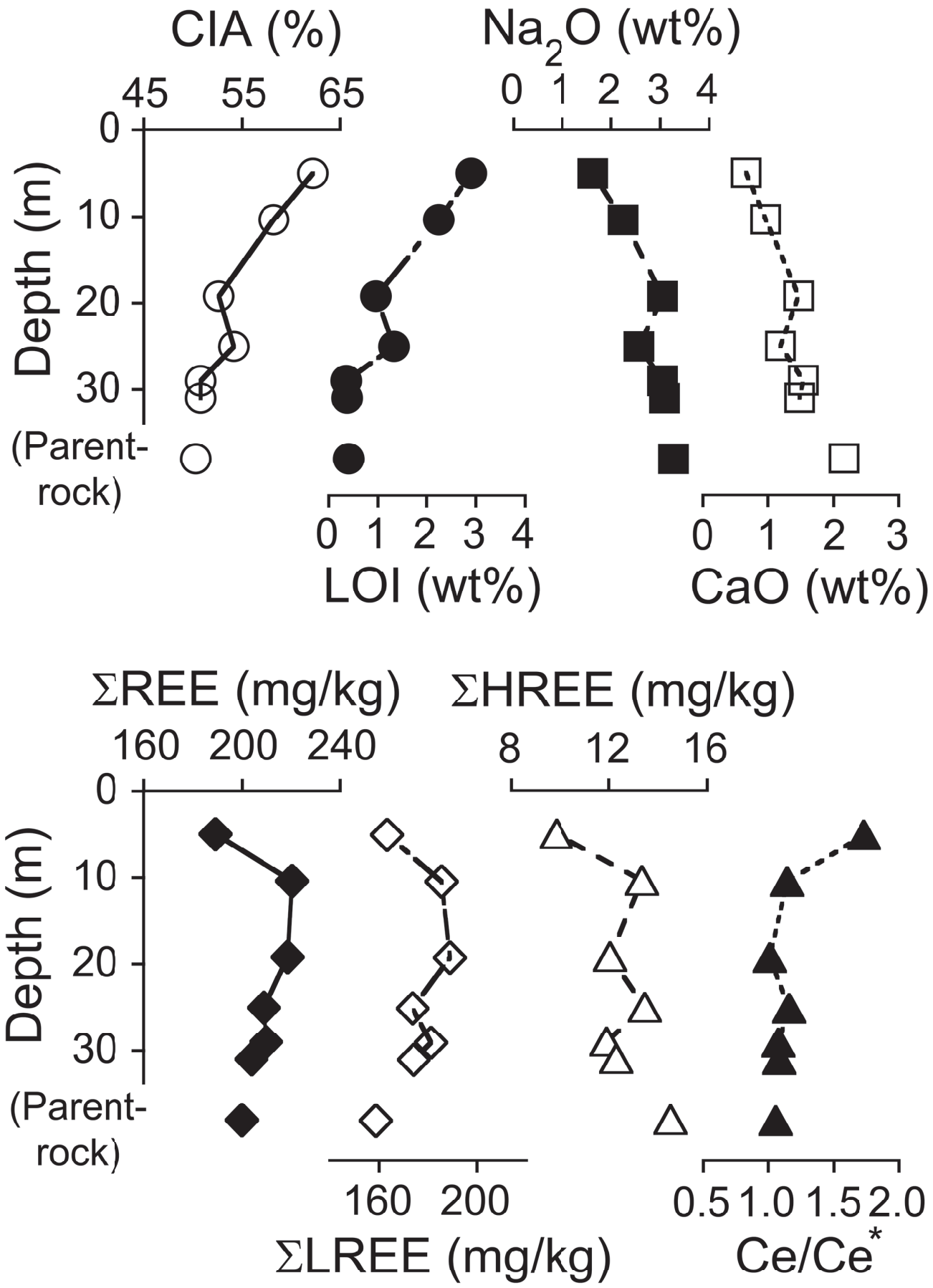

This is a preprint, the final version is subject to change, of the American Mineralogist (MSA)
Cite as Authors (Year) Title. American Mineralogist, in press.
DOI: https://doi.org/10.2138/am-2020-7148

Fig. 3.

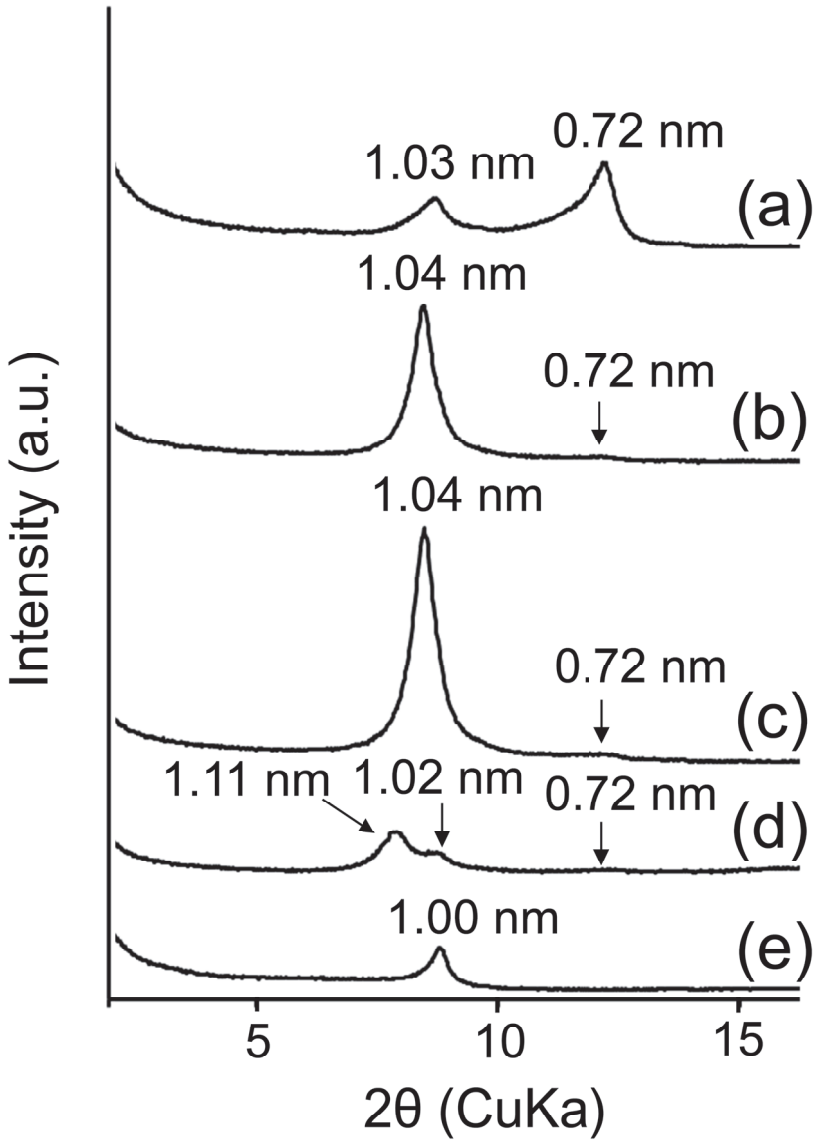

This is a preprint, the final version is subject to change, of the American Mineralogist (MSA)
Cite as Authors (Year) Title. American Mineralogist, in press.
DOI: https://doi.org/10.2138/am-2020-7148

Fig. 4

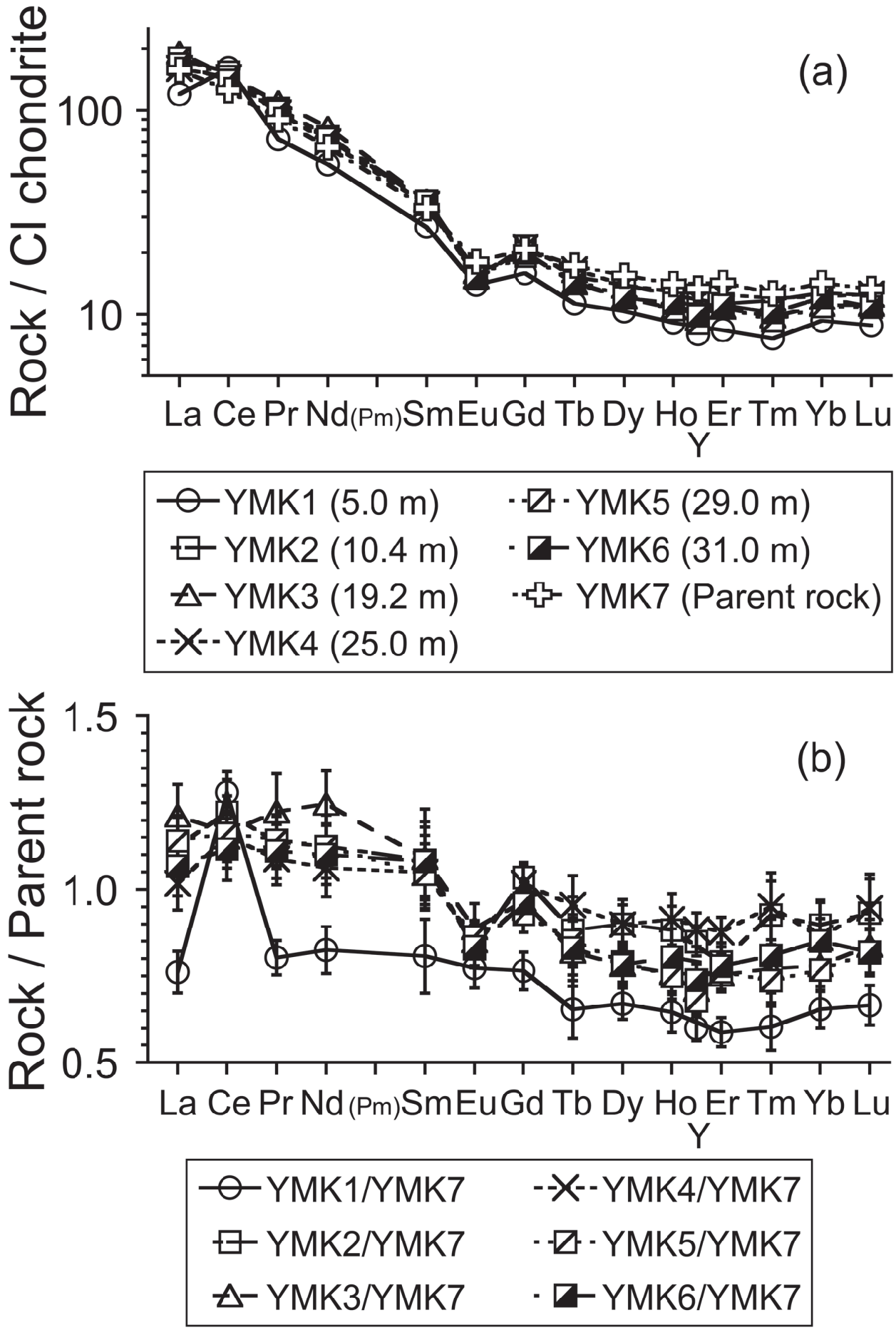

This is a preprint, the final version is subject to change, of the American Mineralogist (MSA)
Cite as Authors (Year) Title. American Mineralogist, in press.
DOI: https://doi.org/10.2138/am-2020-7148

Fig. 5

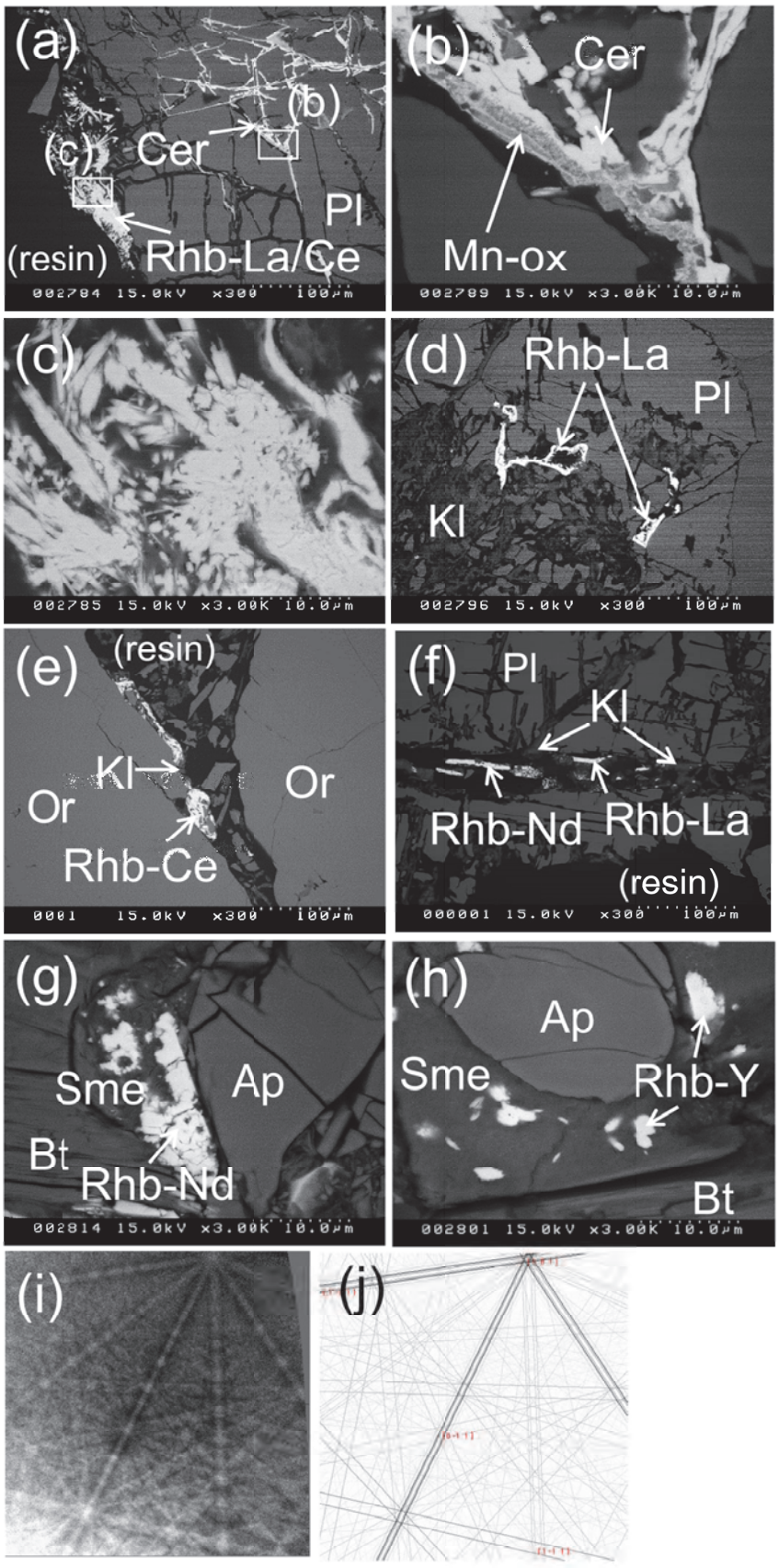

This is a preprint, the final version is subject to change, of the American Mineralogist (MSA)
Cite as Authors (Year) Title. American Mineralogist, in press.
DOI: https://doi.org/10.2138/am-2020-7148

Fig. 6

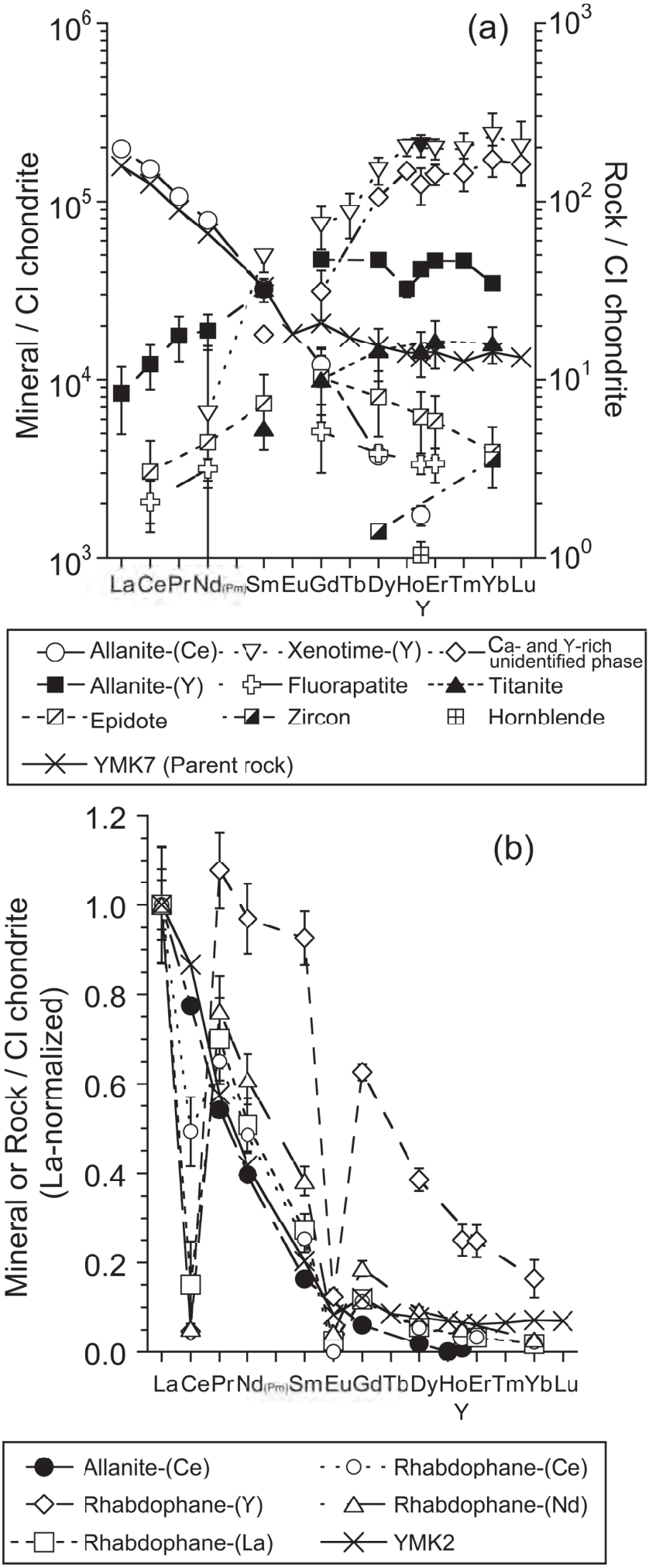

This is a preprint, the final version is subject to change, of the American Mineralogist (MSA)
Cite as Authors (Year) Title. American Mineralogist, in press.
DOI: https://doi.org/10.2138/am-2020-7148

Fig. 7

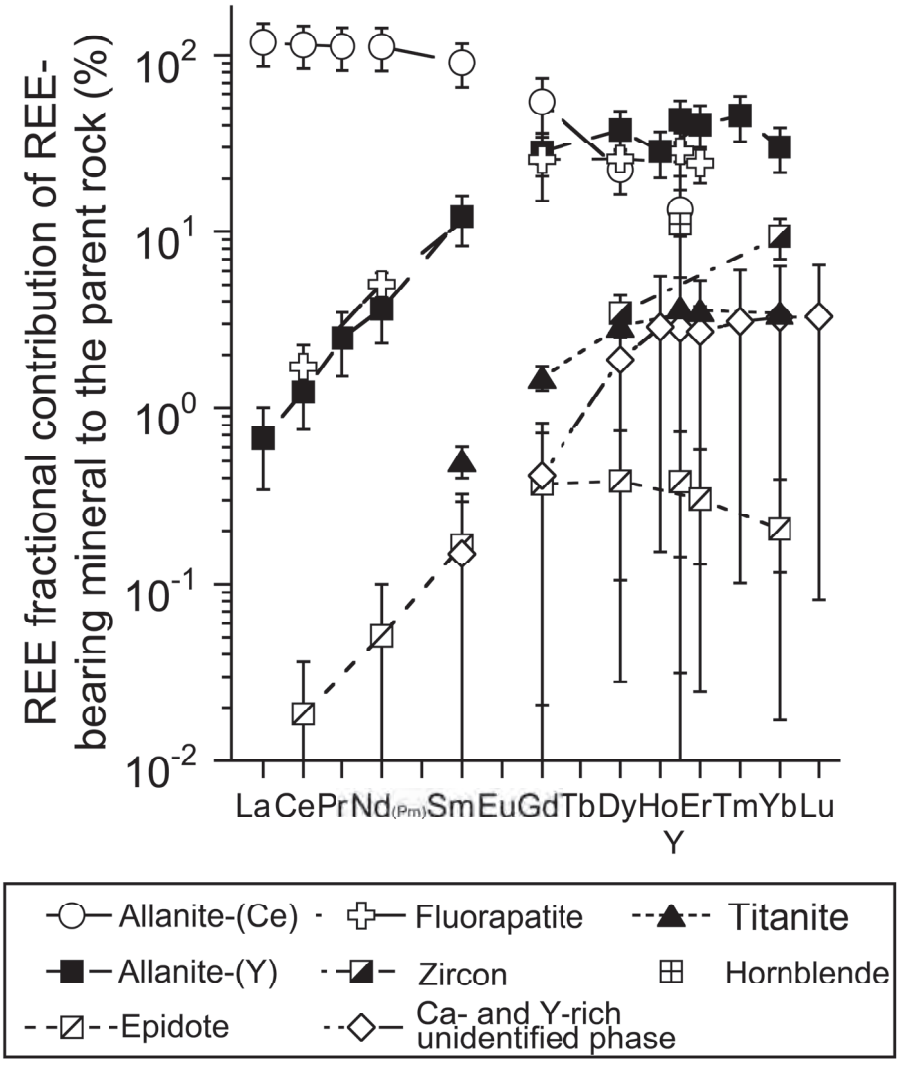

This is a preprint, the final version is subject to change, of the American Mineralogist (MSA)
Cite as Authors (Year) Title. American Mineralogist, in press.
DOI: https://doi.org/10.2138/am-2020-7148

Fig. 8

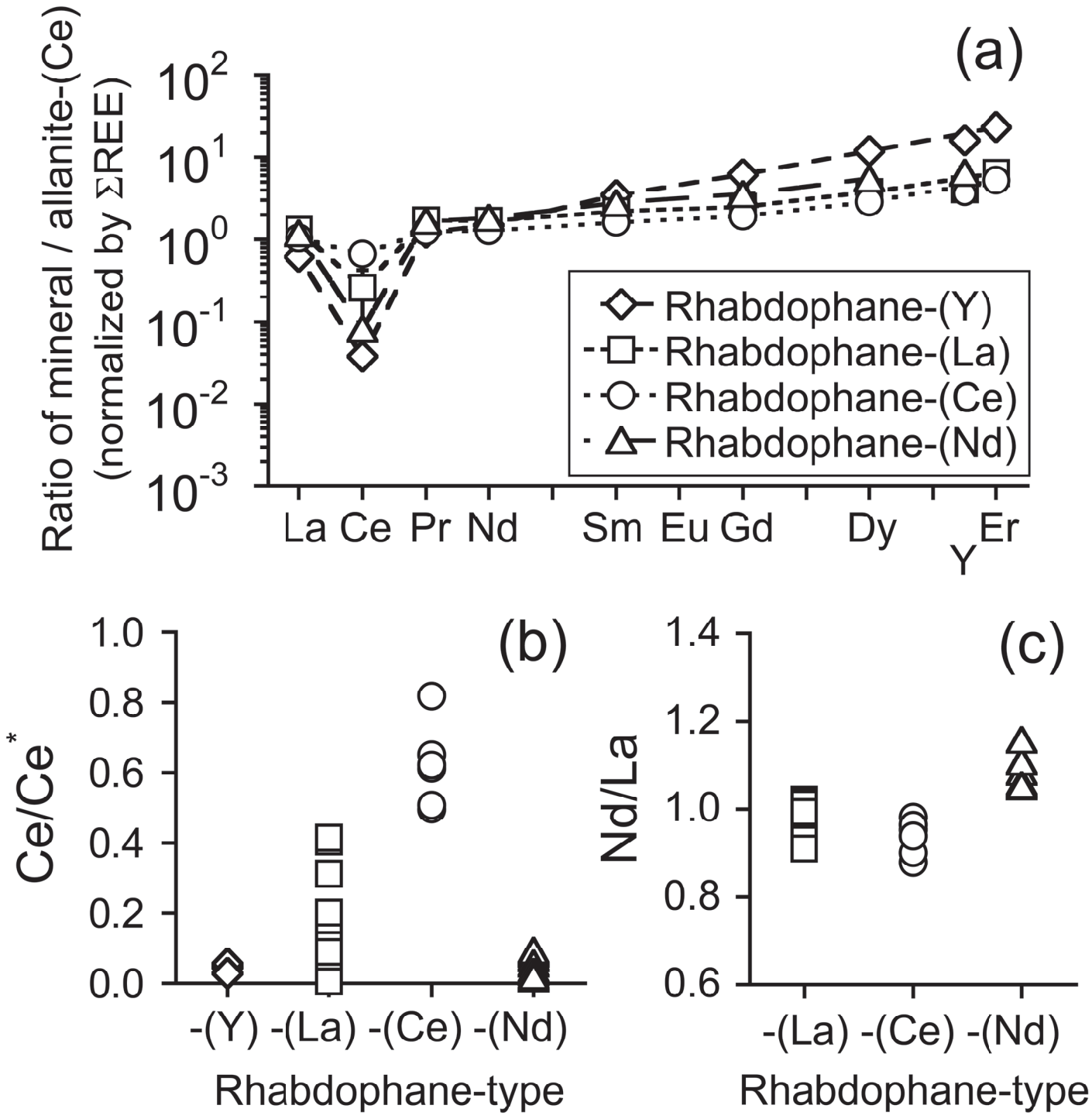

This is a preprint, the final version is subject to change, of the American Mineralogist (MSA)
Cite as Authors (Year) Title. American Mineralogist, in press.
DOI: https://doi.org/10.2138/am-2020-7148

	Mineral in weathered layer	Ce anomaly in bulk layer
Case (i)	Cerianite-(Ce) Rhabdophane (–)	0
Case (ii)	Rhabdophane (–) Cerianite-(Ce), relatively richer	+
	Rhabdophane (–), relatively richer Cerianite-(Ce)	–
Case (iii)	Rhabdophane (~0) Cerianite-(Ce), almost none	0
	Rhabdophane (–) Cerianite-(Ce)	+ or –

Fig. 9